Ballistic Imaging of Transient Phenomena in Turbid Media

Sedarsky, David

2009

Ballistic Imaging of Transient Phenomena in Turbid Media

Doctoral Thesis

David Sedarsky

Division of Combustion Physics
Department of Physics

LUND UNIVERSITY

Lund Reports on Combustion Physics,
LRCP-138
ISRN LUTFD2/TFCP–09/138–SE
ISBN 978-91-628-7963-1

Division of Combustion Physics
P.O. Box 118
SE-221 00 Lund, Sweden

Printed by: Media Tryck AB, Lund, Sweden

Abstract

Ballistic imaging (BI) is a laser-based measurement for enhanced visualization of strong gradient disturbances within inhomogeneous highly scattering media. The technique is a specialized shadow-imaging method, closely related to schlieren and shadowgraph techniques, which focuses on eliminating stray and multiply-scattered source light from a line-of-sight integrated 2-D intensity signal, detected in a forward-collection geometry.

The work presented here is motivated by the challenges to optical diagnostics posed by the dense, multiphase, turbulent flows common in liquid-fueled combustion devices. While spray models continue to improve, fundamental questions remain concerning the fluid dynamic interactions in specific optically dense regions of fuel sprays which are difficult to probe experimentally, due to the high turbidity in these regions. The measurements, analysis, and modeling effort presented in this work directly address this issue, demonstrating that high-resolution spatial information can be obtained even in regions where light signals are severely distorted by scattering.

Experimental investigations of two turbulent sprays were conducted. In the first campaign an air channel and plain-orifice nozzle with a laminar internal flow were used to generate a jet-in-crossflow. BI was applied to characterize the spray and investigate dense areas and voids in the wake region of the flow. The second measurement campaign applied BI to an aerated spray, where breakup was enhanced by adding nitrogen gas to the liquid stream inside the nozzle. Each spray measurement involved a different optical arrangement, providing an opportunity to observe how differences in collection geometry affect the measured spatial intensity.

New spray behavior was observed over the course of both campaigns: The jet-in-crossflow results revealed bifurcation occurring in a two-phase flow field, a phenomenon previously known to occur only in single-phase flows. The aerated spray results showed a range of effervescent breakup behaviors which correlate to the total injection flowrate. To maximize the benefits of BI diagnostics for characterization of transient unsteady phenomena, it is advantageous to acquire large numbers of images such that reliable statistical information can be obtained. As a result, specialized image processing software to analyze ballistic images was developed over the course of the spray characterization campaigns. These software tools and insights pertaining to their application are an important part of this work.

Velocity information is essential for understanding transient phenomena. Hence, there is a strong need to image velocity in dense spray regions. Unfortunately, standard velocity measurements are limited to flow-fields with low turbidity. To address this issue, additional experimental work was undertaken to develop BI as a velocity measurement, applicable to dense sprays. High-resolution ballistic images of a deforming liquid droplet were analyzed, and velocity results for the liquid-gas interface were obtained. Additionally, a fast-framing BI system was constructed at the Propulsion Directorate laboratory and pairs of ballistic images suitable for velocity analysis were obtained for the aerated spray. These image-pairs were successfully analyzed to obtain velocities of individual drops and fluid structures within the flow, resulting in the first demonstration of a dense spray velocity measurement using BI analysis.

A system model for BI diagnostics has been implemented and validated, providing a tool which can quantify and optimize the sensitivity of a BI system applied to a specific scattering environment. Specifically, the model is capable of predicting the average spatial and temporal profile of the transmitted source light for a simulated scattering volume and associated collection and filtering optics. This information provides three main benefits for improving a BI system. First, photon transmission statistics from the model provide reliable insight into how multiple-scattering affects the collected signal for a specific turbid medium. Second, iterative applications of the model allow the optimization of individual optics. Lastly, the model can be used to compute the modulation transfer and point-spread functions for the overall system, allowing the effectiveness of the diagnostic for imaging specific spatial phenomena to be estimated.

List of Papers

This thesis is based on the following papers, which will be referenced by Roman numerals in the text. The papers are referenced and appended to the thesis in the order listed here.

I. Linne, M., Paciaroni, M., Berrocal, E. and **Sedarsky, D.**, *Ballistic Imaging of Liquid Breakup Processes in Dense Sprays*, Proceedings of the Combustion Institute, **32**:2147–2161, 2009

II. **Sedarsky, D**, Paciaroni, M., Petersson, P., Berrocal, E., Zelina, J., Gord, J., and Linne, M., *Model Validation Image Data for the Breakup of a Liquid Jet in Crossflow: Part I*, Experiments in Fluids, (in press)

III. Linne, M., **Sedarsky, D**, Meyer, T., Gord, J., Carter, C., *Ballistic Imaging in the Near-Field of an Effervescent Spray*, Experiments in Fluids, (in press)

IV. **Sedarsky, D**, Paciaroni, M., Linne, M., Gord, J., and Meyer, T., *Velocity imaging for the liquid-gas interface in the near field of an atomizing spray: proof of concept*, Optics Letters, **31**:906–908, 2006

V. **Sedarsky, D**, Gord, J., Carter, C., Meyer, T., and Linne, M., *Fast-framing ballistic imaging of velocity in an aerated spray*, Optics Letters, **34**:2748–2750, 2009

VI. Berrocal, E., **Sedarsky, D**, Paciaroni, M., Meglinski, I., and Linne, M., *Laser light scattering in turbid media Part I: Experimental and simulated results for the spatial intensity distribution*, Optics Express, **15**:10649–10665, 2007

VII. Berrocal, E., **Sedarsky, D**, Paciaroni, M., Meglinski, I., and Linne, M., *Laser light scattering in turbid media Part II: Spatial and temporal analysis of individual scattering orders via Monte Carlo simulation*, Optics Express, **17**:13792–13809, 2009

VIII. **Sedarsky, D**, Berrocal, E., and Linne, M., *Numerical analysis of ballistic imaging for revealing liquid breakup in dense sprays*, Atomization and Sprays, (in press)

Related Work

A. Vestin, F., **Sedarsky, D**, Collin, R., Aldén, M., Linne, M., and Bengtsson, P.-E., *Rotational coherent anti-Stokes Raman spectroscopy (CARS) applied to thermometry in high-pressure hydrocarbon flames*, Combustion and Flame, **154**:143–152, 2008

B. Berrocal, E., Paciaroni, M., **Sedarsky, D**, Meglinski, I., Greenhalgh D., and Linne M., *Validation of a new computational model for multiple scattering of laser radiation in sprays*, Proc. of the 10th International Conference on Liquid Atomization and Spray Systems, Japan, Aug. 27–Sept. 1, 2006.

C. **Sedarsky, D**, Paciaroni, M., Zelina, J., and Linne, M., *Near Field Fluid Structure Analysis for Jets in Crossflow with Ballistic Imaging*, Proc. of the 20th ILASS-Americas, Chicago, Illinois, May 15–18, 2007.

D. Berrocal, E., **Sedarsky, D**, Paciaroni, M. and Linne, M., *Propagation of ultra-short laser light pulses within spray environments*, Proc. of the 20th ILASS-Americas, Chicago, Illinois, May 15–18, 2007.

E. **Sedarsky, D**, Berrocal, E., and Linne, M., *Spatial resolution simulations for time-gating and spatial filtering in ballistic imaging*, Proc. of Laser Applications to Chemical, Security and Environmental Analysis, March, 17–20, 2008.

F. **Sedarsky, D**, Berrocal, E., and Linne, M., *Ballistic imaging for measurement of flow structures in dense multiphase media*, Proc. of the 14th International Symposium on Applications of Laser Techniques to Fluid Mechanics, July 7–10, 2008.

G. **Sedarsky, D**, Gord, J., Kiel, B., Carter, C., Meyer, T., and Linne, M., *Velocity analysis of fluid structures from ballistic images in the near field of an aerated spray*, Proc. of the 10th International Conference on Liquid Atomization and Spray Systems, Vail, Colorado, July 26–30, 2009.

H. Berrocal, E., Kristensson, E., **Sedarsky, D**, Linne, M., *Analysis of the SLIPI technique for multiple scattering suppression in planar imaging of fuel sprays*, Proc. of the 10th International Conference on Liquid Atomization and Spray Systems, Vail, Colorado, July 26–30, 2009.

Contents

Nomenclature

α	multipole radiation coefficient
$\bar{n}_2$	field dependent second-order index of refraction
β	multipole radiation coefficient
$\chi^{(1)}$	linear susceptibility
$\chi^{(3)}$	third-order susceptibility
χ_{eff}	effective susceptibility
δ	phase delay
ℓ	length
ϵ_0	permittivity of free space
$\hat{p}$	polarization vector
λ	wavelength
μ_0	permeability of free space
μ_e	extinction coefficient
ω	angular frequency
ψ	wave function
ρ_f	free charge density
σ_a	aborption cross-section
σ_s	scattering cross-section
τ_0	molecular reorientation time
τ_p	Gaussian pulse duration

ξ	uniform random number
A	amplitude
B	magnetic field
B_{inc}	incident magnetic field
B_{sc}	scattered magnetic field
C	contrast
c	speed of light in vacuum
D	electric displacement field
d	diameter
E	electric field
E_γ	photon energy
E_{inc}	incident electric field
E_{sc}	scattered electric field
f	scattering phase function
f_{Nyquist}	Nyquist frequency
H	auxiliary magnetic field
h	Planck's constant
h_l	spherical Bessel function
I	irradiance
I_f	final intensity
I_i	initial intensity
I_{min}	maximum intensity
I_{min}	minimum intensity
J_f	free current density
j_l	spherical Bessel function
k	Boltzmann constant
k	wavevector

L	angular momentum operator
L	radiance
l_{fp}	free path length
n	index of refraction
n_0	linear index of refraction
n_2	intensity dependent second-order index of refraction
N_V	particle number density per unit volume
OD	optical depth
P	electric polarization density
p_γ	photon momentum
q	Mie scattering size parameter
Q_L	liquid flowrate
r	radial position vector
r_p	Gaussian beam waist
S	Poynting vector
s	direction unit vector
T	period
T	temperature
t	time
v	speed
$X_{l,m}$	vector spherical harmonic function
$Y_{l,m}$	vector spherical harmonic function
A	albedo
GLR	gas-to-liquid ratio
Re	Reynolds number
We	Weber number

List of Figures

List of Tables

Chapter 1

Introduction

This work specifically concerns the task of measuring transient information in environments which are not amenable to standard imaging due to distortion of the optical signal by scattering within the measurement volume. In essence, the aim is to see through an optical disturbance, such as fog, smoke, or a haze of droplets, to produce time-resolved, high-resolution images of something inside.

To this end, a laser-based spatial intensity measurement, termed ballistic imaging (BI), is examined. The technique is a specialized shadow-imaging method designed for resolving structure inside highly scattering media. The diagnostic works by illuminating the measurement volume with collimated light from an ultrafast ($\sim$100 fs) laser pulse and collecting the light that scatters through the measurement volume in the forward direction. The light collection is arranged such that a particular subset of the transmitted light which is minimally affected by scattering is collected by the system, i.e. a large portion of the actual signal is discarded, leaving a small part of the original intensity with spatial information that differs from the bulk signal. The resulting image is formed with a fraction of the total light intensity that passes through the measurement volume, but with improved image contrast, thereby revealing internal structures.

Due to the widespread use and global impact of combustion, the imaging of fuel sprays used in liquid-fueled combustion devices is an application of particular interest. The use of liquid fuels is ubiquitous, especially in transportation applications, because liquid fuels contain much more energy per unit volume than gas-phase fuels. The magnitude of this difference in energy is illustrated by Fig. 1 which shows the energy density of a number of gaseous and liquid phase fuels common in combustion applications. To burn any liquid fuel at an effective rate, it is necessary first to convert the liquid stream into a vapor stream and mix the vapor with a suitable oxidizer using a fuel spray.

Here, the fluid dynamics associated with the breakup and mixing of the injected liquid with the surrounding gas is often obscured by an ambient cloud of droplets, rendering conventional methods such as shadowgraphy or planar imaging ineffective. By applying BI, the dense regions of fuel sprays can be probed directly.

In most liquid-fueled combustion devices, the dynamics of liquid breakup domi-

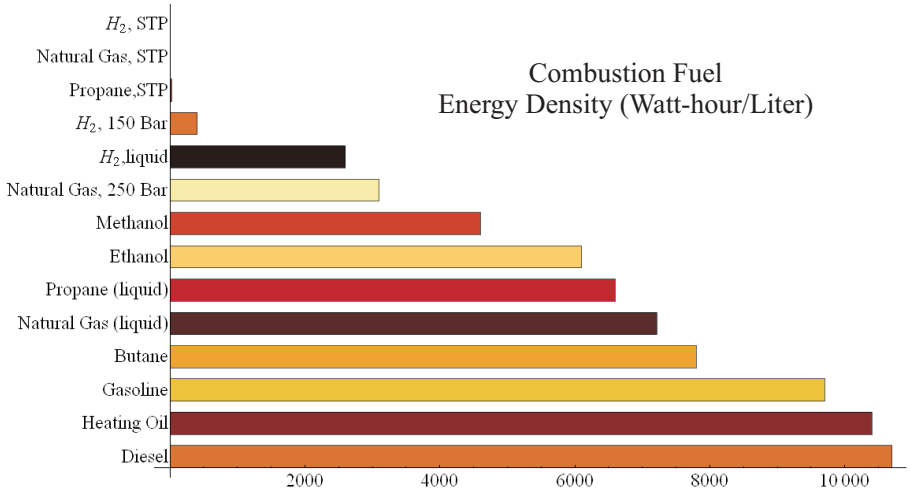

Figure 1.1: *Volumetric energy density of various gas and liquid phase combustion fuels.*

nate mixing in the reaction zone, and are therefore directly coupled to the combustion reaction. As a result, understanding the fluid dynamics of spray breakup is essential for the design of efficient combustion devices. Although models describing fuel injection continue to improve, fundamental questions remain concerning the specific processes and forces which drive liquid breakup. Clear measurements of liquid/gas boundaries and fluid structures in dense spray regions directly address these questions and further provide the potential for spray model validation. This work is primarily motivated by the need for these measurements.

The following four chapters introduce both modeling and experimental results developed over the course of this thesis work. Chapter 2 introduces some of the concepts which are fundamental to understanding light propagation, scattering from single particles, and the modeling approach explained in Ch. 5. Chapter 3 introduces some terminology and explains the idea behind ballistic imaging. A brief outline of previous work is given, followed by a short discussion of the main types of light discrimination used to achieve BI. Chapter 4 introduces both of the spray systems studied in the course of this work and details the BI arrangements that were used in each of the experiments. Chapter 5 presents the BI system model. The major parts of the system model are explained and numerical results from the model are compared with measurements from the literature made on solutions of polystyrene microspheres.

Chapter 2

Background Physics

This chapter briefly reviews some fundamental concepts that are relevant to light propagation, imaging, and scattering from large particles. The intent is to briefly introduce the basis for the properties of light, and the conceptual tools which enable an accurate description its interaction with an optical system and scatterers within a turbid medium.

2.1 Maxwell's equations

Light is characterized by it's energy, intensity, polarization, and coherence and is intimately connected to the motion and disposition of charge, i.e., light is a manifestation of electromagnetic interaction. The fundamental relationships governing electricity and magnetism can be stated concisely by a set of four coupled, first-order, partial differential equations[6]:

$$\bigtriangledown \cdot D = \rho_f \tag{2.1}$$

where D is the electric displacement field in units of coulombs/meter^2 and ρ_f is the free charge density,

$$\bigtriangledown \cdot B = 0 \tag{2.2}$$

where B is the magnetic field in units of volt-second/meter^2,

$$\bigtriangledown \times E = -\frac{\partial B}{\partial t} \tag{2.3}$$

where E is the electric field in units of volts/meter, B is the magnetic field, and t is time,

$$\bigtriangledown \times H = \frac{\partial D}{\partial t} + J_f \tag{2.4}$$

where H is the auxiliary magnetic field in units of Ampere/meter, D is the electric displacement field, t is time, and J_f represents the free current density.

These relations are known collectively as Maxwell's equations, and individually designated Gauss's law, Gauss's law for magnetism, Faraday's law of induction, and Ampére's law with Maxwell's correction, respectively. If the region of interest contains no free charges ($\rho_f = 0$), no free currents ($J_f = 0$), and is nonmagnetic, the electric field, E, and the magnetic field, B, are related to D and H by:

$$D = \epsilon_0 E + P \tag{2.5}$$

$$B = \mu_0 H \tag{2.6}$$

Where ϵ_0 is the permittivity of free space in farads/meter and μ_0 is the permeability of free space in Newtons/Ampere^2. P is the electric polarization density, or dipole moment per unit volume, of the material system, and depends in a nonlinear fashion on the strength of the electric field.

2.2 Electromagnetic wave equation

By manipulating Maxwell's equations, a relation can be formed which allows the electric and magnetic fields to be examined in detail. Taking the curl of Eq. 2.3, which describes how a changing magnetic field gives rise to an electric field, and combining the result with Eq. 2.4 and Eq. 2.6 yields the relation:

$$\bigtriangledown \times \bigtriangledown \times E + \mu_0 \frac{\partial^2}{\partial t^2} D = 0 \tag{2.7}$$

Recalling an identity from vector calculus,

$$\bigtriangledown \times \bigtriangledown \times v = \bigtriangledown(\bigtriangledown \cdot v) - \bigtriangledown^2 v \tag{2.8}$$

and applying Eq. 2.5 to eliminate D, Eq. 2.7 can be rewritten as:

$$\bigtriangledown (\bigtriangledown \cdot E) - \bigtriangledown^2 E + \mu_0 \epsilon_0 \frac{\partial^2}{\partial t^2} E = -\mu_0 \frac{\partial^2}{\partial t^2} P \tag{2.9}$$

Assuming the divergence of E is negligible, the first term drops out of Eq. 2.9, yielding a partial differential equation in the form of a wave equation with a characteristic propagation speed of $c = 1/\sqrt{\mu_0 \epsilon_0}$, and a source term resulting from the polarizability of the system interacting with the fields

$$\bigtriangledown^2 E + \frac{1}{c^2} \frac{\partial^2}{\partial t^2} E = \frac{-1}{\epsilon_0 c^2} \frac{\partial^2}{\partial t^2} P \tag{2.10}$$

A similar approach starting from Eq. 2.4 leads to another wave equation describing the magnetic field B:

$$\bigtriangledown^2 B + \frac{1}{c^2} \frac{\partial^2}{\partial t^2} B = \frac{-\mu_0}{\epsilon_0 c^2} \frac{\partial^2}{\partial t^2} P \tag{2.11}$$

Both of these wave equations admit general solutions [40] of the form:

$$\psi(s,t) = \sum_{j=1}^{3} f(s_j - ct) + g(s_j + ct) \tag{2.12}$$

Here, s_j represents each spatial dimension and the arbitrary functions f and g represent traveling waves which move in opposite directions with velocity c.

The significance of this result is that the form and behavior of electromagnetic fields are accurately described by solutions to this wave equation, subject to the constraints of Maxwell's equations. Consequently, light can be treated as coupled, transverse, mutually perpendicular electric and magnetic waves propagating in space and time.

2.3 Wave insights

A particularly useful solution to the wave equation is given by a sinusoidal wave. Over a single spatial dimension, x, this solution can be written as

$$\psi(x,t) = A\cos\left(\frac{2\pi}{\lambda}(x - vt) + \delta\right) \tag{2.13}$$

where A represents the amplitude of the wave, λ is the wavelength, v is the speed of the waveform, and δ is the phase delay. By defining the wavevector, period, and angular frequency,

$$k = \frac{2\pi}{\lambda}, \quad T = \frac{2\pi}{kv}, \quad \omega = kv \tag{2.14}$$

and applying Euler's formula

$$e^{i\phi} = \cos\phi + i\sin\phi \tag{2.15}$$

Eq. 2.13 can be written in the familiar complex exponential form for a harmonic wave, given by

$$\tilde{\psi}(x,t) = \tilde{A}e^{i(kx-\omega t)} \tag{2.16}$$

where $\tilde{A} = Ae^{i\delta}$, and the physical form of the wave is understood to be the real part of $\tilde{\psi}$.

By inspecting form of Eq. 2.12, one can see that the sum of two solutions is also a valid solution to the wave equation. This property is known as the superposition principle and has the consequence that when two separate waves overlap, they will interfere such that the field in the region of overlap is the algebraic sum of the the individual waves. This property of waves is illustrated in Fig. 2.3 which shows the interference pattern resulting from the combination of sine waves generated by separate point sources in a wave tank.

By itself, the harmonic wave solution given in Eq. 2.16 represents one specific waveform. However, according to the principles of Fourier analysis, arbitrary waveforms can

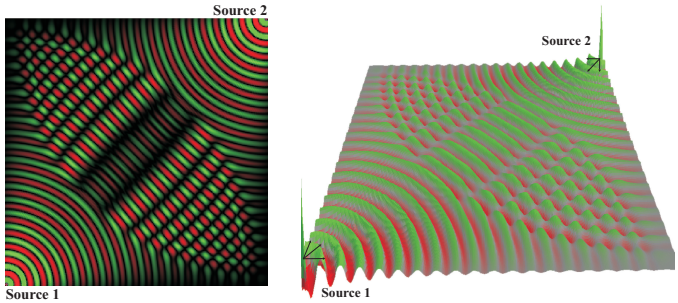

Figure 2.1: *2D (left) and 3D (right) views of the superposition of waves from two point sources oscillating at the same frequency.*

be represented by an appropriate linear combination of sinusoidal waves. Since the sum of two or more solutions is itself a solution, a sum of solutions in the form of Eq. 2.16 can be used to describe behavior of any wave.

Applying the solution given by Eq. 2.16 to Eqs. 2.10 and 2.11 in free space or a uniform dielectric environment, such that the source terms on the right hand side vanish, yields a plane wave representation of the electric and magnetic fields

$$\tilde{E}(x,t) = \tilde{E}_0 e^{i(kx-\omega t)} \tag{2.17}$$

$$\tilde{B}(x,t) = \tilde{B}_0 e^{i(kx-\omega t)} \tag{2.18}$$

In this case, the light wave propagates in the x-direction and is uniform over every plane perpendicular to the x-axis.

By examining properties of waves other important aspects of light can be deduced. Transverse waves oscillate with a particular orientation. They exhibit a handedness, or pattern associated with their mode of vibration, which strongly influences the way the waves interact with their environment. This specific mode of a wave's oscillation is commonly referred to as the polarization of the wave. This property can be visualized by picturing the transverse wave from a head-on perspective (positioned on the axis of propagation looking in the direction of the oncoming wave) and following an arbitrary point on the wave as it precesses about the axis of the direction of propagation. Since there are two dimensions perpendicular to any given line of propagation, the polarization can be described by a vector, $\hat{p}$, defining the plane of vibration in terms of the polarization angle.

$$\hat{p} = \cos\theta\hat{\jmath} + \sin\theta\hat{k} \tag{2.19}$$

Accordingly, the plane wave introduced in Eq. 2.16 can be viewed as a linear combination of vertically and horizontally polarized components given by

$$\tilde{\psi}(x,t) = \left(\tilde{A}\cos\theta\right) e^{i(kx-\omega t)}\hat{\jmath}\left(\tilde{A}\sin\theta\right) e^{i(kx-\omega t)}\hat{k} \tag{2.20}$$

Combining Eqs. 2.19 and 2.17 yields the electric field for a monochromatic plane wave with an arbitrary polarization angle, θ:

$$\tilde{E}(x,t) = \left(\tilde{E}_0 \cos\theta\right) e^{i(kx-\omega t)}\hat{\jmath} \left(\tilde{E}_0 \sin\theta\right) e^{i(kx-\omega t)}\hat{k} \tag{2.21}$$

This solution to the wave equation represents a convenient and analytically tractable approximation for the collimated source light produced and utilized in many optical systems, and has a special bearing on light scattering in optically dense media.

2.4 Photon insights

To this point, the discussion regarding the nature of light has been based on the observation of macroscopic trends. However, it is important to realize that light is fundamentally a quantum phenomenon. The earlier experimental work of Planck and theoretical work of Einstein on the photo-electric effect showed convincingly that light is composed of distinct entities. Each of these light particles, known as photons, carry a quantized amount of energy related directly to the wavelength of the light by

$$E_\gamma = hc/\lambda \tag{2.22}$$

where h is Planck's constant, c is the speed of light in vacuum, and λ is the wavelength of the monochromatic electric field which describes the photon. Individual photons interact with the world as indivisible point-like entities. Photons travel at the speed of light and are therefore constrained by the theory of relativity to have zero rest mass. Compton's work with x-ray scattering showed that photons also carry momentum which is directly related to the wavelength of the light by

$$p_\gamma = h/\lambda \tag{2.23}$$

and obey momentum and energy conservation much like particles with non-zero rest mass.

Careful measurements of light show that photons obey Bose-Einstein statistics, implying that the quantum mechanical states of a collection of identical photons must be symmetric and the statistical weight of a state containing n photons is 1. The state for an individual photon or collection of identical photons can be represented by a properly normalized solution to Maxwell's equations.

The irradiance, I, refers to the amount of light incident on a surface and is defined as the average energy per unit area per unit time. The Poynting vector, given by:

$$S = c\epsilon_0 E \times B \tag{2.24}$$

describes the flow of electromagnetic energy through a surface, such that the time-averaged magnitude of the this energy flow represents a measure of I,

$$I = \frac{c\epsilon_0}{2} E_0^2 \tag{2.25}$$

In effect, a light wave is a massive collection of point-like particles, where the photon is the basic unit, or carrier of energy. Since the irradiance given in Eq. 2.25 is proportional to the square of the amplitude of the electric field and simultaneously proportional to the number of photons, the number of photons must also be proportional to $\langle E^2 \rangle$. Hence, the square of the field strength can be interpreted as a measure of the probability of finding a photon for a given location in time and space.

2.5 Mie scattering

The manner in which light scatters from single particles can be solved analytically by applying the plane wave representation of the electric and magnetic fields to an isolated sphere contained in a uniform dielectric medium. Conceptually, one can imagine the incident light wave induces currents within the sphere, causing it to radiate. The interior of the sphere contains this generated field and the region surrounding the sphere contains a scattered field which is the superposition of the incident and generated fields. The complete description of the scattered field can be obtained in terms of a multipole expansion of the incident electric and magnetic fields.

Scattering of this form is termed Lorenz-Mie-Debye scattering, or more commonly Mie-scattering, after the first authors to publish the solution for scattering of a plane wave by a dielectric sphere. A detailed treatment of this arrangement is given by Born and Wolf [6]. A qualitative outline of the procedure is given here which borrows the notation and form of the derivation given by Jackson [26].

Consider a sphere with a uniform dielectric constant, ϵ, centered at the origin and surrounded by medium with dielectric constant, ϵ_0. First, the incident plane wave fields are rewritten in spherical coordinates as Debye potentials [18] in terms of the differential angular momentum operator

$$L \equiv (1/i) r \times \bigtriangledown$$

Continuity conditions at the boundary of the sphere are imposed on the E and B Debye potentials, which are expanded in terms of the vector spherical harmonics

$$X_{l,m} \equiv L Y_{l,m} / \sqrt{l(l+1)}$$

and spherical Bessel functions, $j_l(k_0 r)$, to give

$$E_{inc}(r) = E_0 \sum_{l=1}^{\infty} i^l \sqrt{4\pi(2l+1)} \left(j_l(k_0 r) X_{l,\pm 1} \pm \frac{1}{k_0} \bigtriangledown \times j_l(k_0 r) X_{l,\pm 1} \right)$$

$$B_{inc}(r) = \pm i \sqrt{\epsilon_0} E_{inc}(r)$$

The scattered fields can be expressed with similar expansions, with the additional constraint that they contain Bessel functions, $h_l^{(l)}(k_0 r)$, which specify purely outward propagating waves, to satisfy the boundary condition of the scattered wave at infinity. The

scattered fields are given by

$$E_{sc}(r) = \frac{E_0}{2} \sum_{l=1}^{\infty} i^l \sqrt{4\pi(2l+1)} \left(\alpha_{\pm}(l) h_l^{(l)}(k_0 r) X_{l,\pm 1} \pm \frac{\beta_{\pm}(l)}{k_0} \bigtriangledown \times h_l^{(l)}(k_0 r) X_{l,\pm 1} \right)$$

$$B_{sc}(r) = \frac{E_0 \sqrt{\epsilon_0}}{2} \sum_{l=1}^{\infty} i^l \sqrt{4\pi(2l+1)} \left(\frac{-i\alpha_{\pm}(l)}{k_0} \bigtriangledown \times h_l^{(l)}(k_0 r) X_{l,\pm 1} \mp i\beta_{\pm}(l) h_l^{(l)}(k_0 r) X_{l,\pm 1} \right)$$

where the coefficients α and β characterize the amplitudes of the magnetic and electric multipole radiation. The interior fields are derived in a similar manner, with the constraint that they contain Bessel functions, $j_l(k_0 r)$, which are nonsingular at the origin. At this point the fields are specified at all points, and the coefficients for the amplitude of the multipole radiation can be computed by enforcing the continuity of the interior and scattered fields at the surface of the sphere.

The resultant scattered wave is written as an infinite series in the vector spherical harmonics. These are the normal modes of the spherical particle which impart a natural angular dependence to the field [5]. This mode structure is weighted by the appropriate coefficients, α and β, which depend explicitly on

- the ratio of refractive index between the particle and the medium
- a size parameter, $q = 2\pi nd/\lambda$, relating the diameter of the particle, d, the wavelength, λ, of the incident light wave, and the refractive index of the medium, n.

The resulting scattering phase functions for 1, 5, and 20 micron polystyrene spheres are shown in Fig. 2.5. The normalized scattered light intensity detected in the back, side, and forward detection geometries for each of these particle sizes is shown in Fig. 2.4. Note that the scattered intensity profiles are radially symmetric, although the detected spatial intensities are distorted slightly by the detection arrangement, which utilizes flat detector regions (see Fig. 2.2).

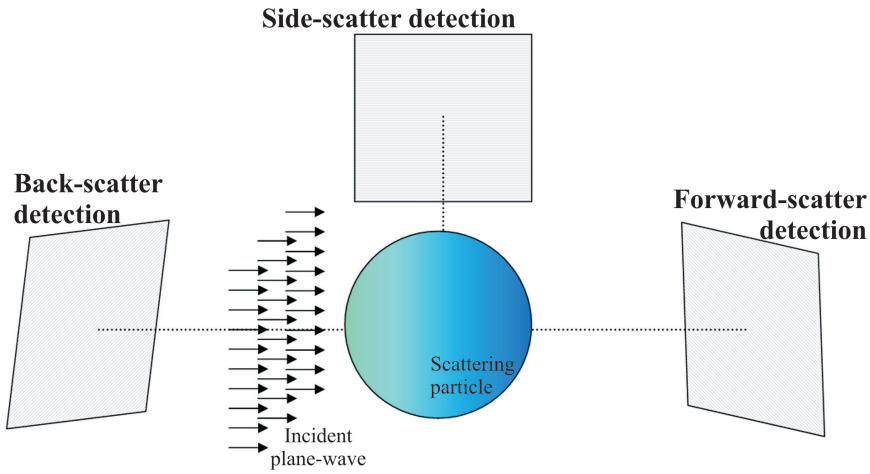

Figure 2.2: *Diagram of back, side, and forward detection planes arranged normal to the surface of an isolated sphere to view the light scattering induced by an incident plane wave.*

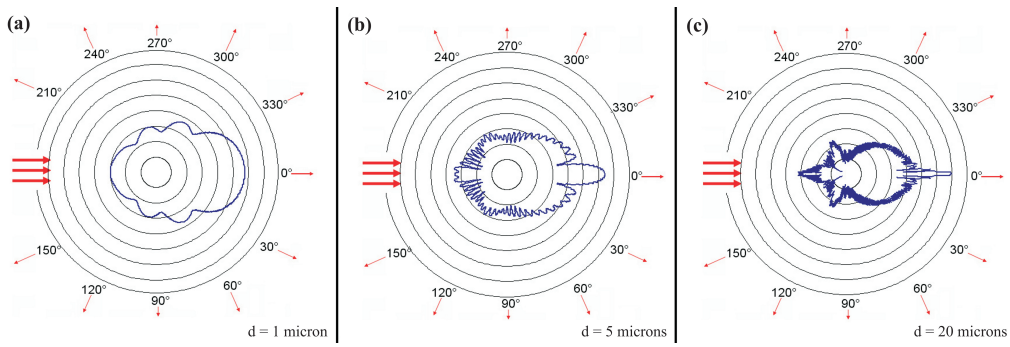

Figure 2.3: *Polar phase functions for plane-wave scattering from an isolated polystyrene microsphere for particle sizes: d = 1, 5, and 20 μm (logarithmic scale).*

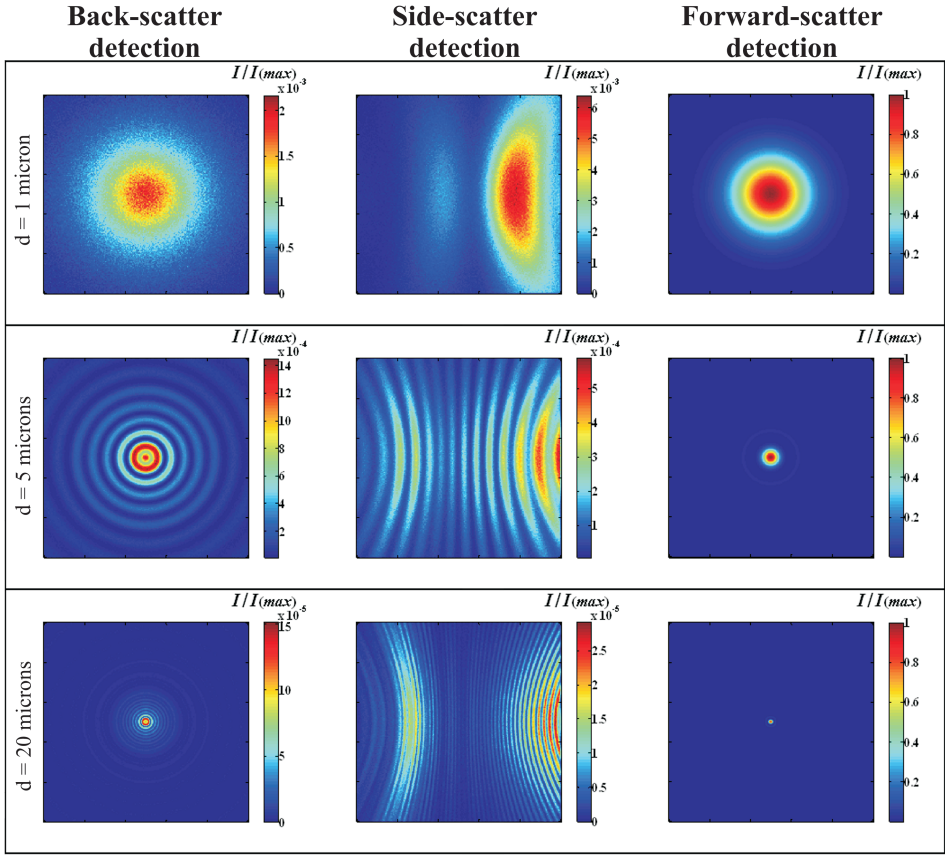

Figure 2.4: *Intensity of back, side, and forward plane-wave scattering from a single polystyrene sphere for particle diameters: d = 1, 5, and 20 microns. The phase functions describing these interactions are shown in Fig. 2.5. The detection arrangement for each of the three views is shown in Fig. 2.2.*

2.6 Rays and photon packets

A ray is a rectilinear path along the central axis of a beam-like collection of photons which can be used to track the location and evolution of various properties associated with a group of photons. In the limit where the apertures and components of an optical system are large compared to the wavelength and the diameter of a beam of light, the behavior of the group of photons which compose that light can be estimated by tracing the trajectory of the light beam through the system using a series of rays.

The most common application of rays is the tracing of source light through an optical system using the rules of geometric optics, which account for reflection and refraction at surfaces but do not account for the effects of diffraction. This approach yields perfectly conjugate object and image spaces and tracks only the straight-line trajectories between surfaces.

Ray trace analysis is not intrinsically limited to geometric optics, however. The technique can be extended by including more detailed behavior related to the properties of light tracked by each ray. For example, by tracking the polarization state for the light modeled in each ray and incorporating Jones calculus in the rules for ray/surface interactions, polarization effects can be calculated [43].

Rays can be used to model the propagation of light through an optical system by sectioning the source light into discrete spatially coherent packets that can be computationally propagated through the system by rules governing the average behavior of the source light defined over each light packet. In this manner, ray tracing can function as a path tracking tool that samples the wavefront of the light source at each surface along the optical path. The numerical model presented in Ch. 5, which treats light propagation through a complete BI instrument, is predicated on a simple implementation of this concept.

2.7 Summary

The purpose of this chapter was to review some of the essential concepts regarding the nature and description of light in order to clarify the modeling approach introduced in Ch. 5, which is used to describe a complete BI system. The important conclusions of this chapter are summarized below.

- Light can be rigorously treated as wavefunction or set of wavefunctions which describes a group of photons in terms of the probability for detecting a photon at a given time and place.
- Scattering from single particles strongly resembles the phase function for the scattered field determined by the Lorenz-Mie-Debye theory, which is a function of particle size, relative refractive index, and source light wavelength.
- In the limit where the wavelength and diameter of a beam-like group of photons is small compared to the size of the components of the optical system, rays can be used to estimate the wavefront generated by a well-defined light source.

Chapter 3

Ballistic imaging

The following sections briefly outline the history of ballistic imaging (BI) diagnostics, define the principles of the technique, and summarize some of the methods discussed in the literature which have been used to implement BI systems.

3.1 History

The term *ballistic imaging* is used in the medical imaging community to describe a diverse group of optical diagnostic applications investigated for their ability to mitigate the effects of optical interference often encountered in transillumination imaging of biological tissues [2].

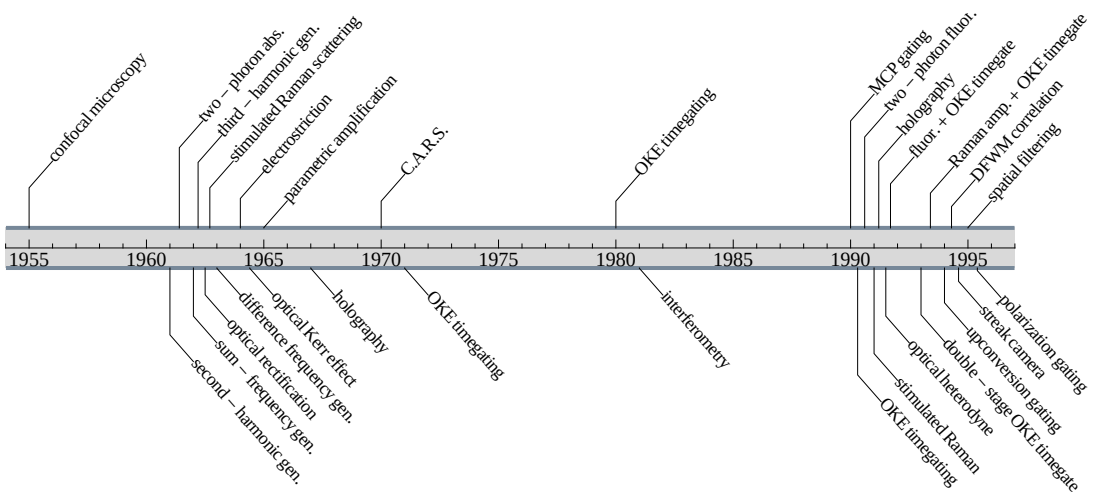

Figure 3.1: *Time history of research related to ballistic imaging.*

Here, the feature or object of interest is embedded in a medium (human breast tissue, for example) where a significant fraction of the source light is redirected by scattering within the medium. In simple terms, the optically dense space surrounding the region of interest acts as a diffuser, which severely alters the spatial intensity information detected from the image plane.

Most of the medical applications of BI appeared in the 1990's due, in large part, to the combination of newly available laser sources, fast detectors, and two-dimensional array cameras. However, these diagnostic efforts built on significant work in physics and optics which occurred decades earlier. The timeline in Fig. 3.1 highights research in optics and biomedical diagnostics related to the development of BI.

Early efforts to adapt microscopy for imaging in optically thick media led to the development of confocal microscopy [42], which utilizes point-wise illumination and detection and apertures near the object plane to minimize multiply-scattered light generated in the sample. In 1960, the ruby laser was introduced, followed shortly by the demonstration of a host of nonlinear optics phenomena including:

- second-harmonic generation
- two-photon absorption
- sum-frequency generation
- stimulated Raman scattering
- difference frequency generation
- the optical Kerr effect
- parametric amplification
- coherent anti-Stokes Raman scattering

Each of these nonlinear effects exhibit potential for segregating light based on the properties of its constituent photons.

As early as 1962, work by Leith and Upatneiks [33] demonstrated the possibility of correcting image distortion using holographic methods. In 1967, Stetson [56] published a letter noting how an off-axis reference-beam hologram, essentially performing coherence gating, was able to improve the image quality of an object immersed in a colloidal solution of milk or soap.

In 1969, Duguay and Hansen developed an optical Kerr effect (OKE) shutter [11]. Two years later Duguay and Mattick [12] published the first BI work exploiting the optical Kerr effect for time-gated imaging and suggested that their optical arrangement might be suitable for imaging through biological tissues.

Almost a decade later, Martin et al. [41] built an OKE shutter based on Duguay's design and applied the system in a time-gated backscattering arrangement to image several biological systems, including structures inside a beef heart. In 1986, Fujimoto and co-workers applied an similar system to image internal structures of a rabbit eye.

In the 1990's a large amount of work was published exploring holography [1, 23, 31, 32, 53], polarization gating [10, 15, 17, 21, 35, 52, 58], nonlinear coherence gating methods [3, 13, 39, 49, 54, 64, 65], and OKE time-gating [27, 34, 61, 62]. A useful summary of BI literature spanning this time period was given by Paciaroni [45], and a thorough review was provided by Dunsby and French [14] in 2003.

The earliest spray measurements applying BI were reported by Galland et al. in 1995 [16]. They applied an OKE shutter driven by 8 ps pulses to obtain images of a water jet in a LOx combustor chamber, with a spatial resolution on the order of 0.5 mm. In 2004, Paciaroni and Linne [47] redesigned this system adding improved optics and an OKE shutter driven by 80 fs pulses, resulting in a spatial resolution on the order of 50 μm for dense sprays.

3.2 Definition of ballistic imaging

The goal of a ballistic imaging (BI) application is to obtain high-resolution spatial information from within a turbid, or "optically thick" region, where the source light is severely distorted by scattering within the measurement volume. This is accomplished by judiciously limiting light collection, allowing the formation of images with increased contrast using a small subset of the total light intensity. In other words, a large portion of the actual signal is purposely discarded, leaving a small part of the original intensity with spatial information that differs from the bulk signal. The name for the technique stems from the concept that, even when transiting highly scattering media, some amount of light penetrates the medium without participating in scattering interactions which discernibly change its properties. This "ideal" signal, commonly referred to as *ballistic* light, is attenuated in turbid media according to the Beer-Lambert relation [4],

$$I_f = I_i e^{-N_V(\sigma_s+\sigma_a)\ell} \tag{3.1}$$

which describes the reduction of the incident irradiance, I_i, by interaction with particles over a distance, l, where N_V is the particle number density per unit volume, and σ_s and σ_a represent the particle scattering and absorption cross-sections. To get an estimate of the turbidity of a medium one often defines the extinction coefficient, μ_e, or the optical depth,

$$OD = N_V(\sigma_s + \sigma_a)\ell = \mu_e\ell \tag{3.2}$$

As the optical depth increases, the ballistic signal falls off exponentially. Since ballistic light retains its properties in transit, this light can be segregated from transmitted light which is substantially altered by the medium, and used to form a high-resolution image.

The overall goal is to separate the information carrying photons from the diffusely scattered photons which contribute predominately image noise and obscure the signal of interest. In general, it is not possible to separate the information carrying and noise photons in absolute terms. However, a detailed understanding of how turbid media alters the properties of source light can indicate effective means of discriminating noise photons based on their altered properties. A wide variety of light filtering methods are possible; the accuracy and limitations of each method naturally depend on the light properties they exploit for discrimination, and the specifics of the scattering medium.

The present work is concerned with imaging arrangements which can be effectively applied to study the fluid dynamics of transient multi-phase flows. Of specific interest are the complex fluid mechanical structures and dynamics of high-pressure atomizer

sprays. Although a slightly larger variety of light filtering methods are mentioned, the focus of the discussion and work presented here is on imaging systems which:

- collect light in a forward-scatter geometry
- generate a two-dimensional spatial intensity signal without scanning
- are capable of single-shot, or time-resolved measurements

3.3 Light collection

In an ideal imaging situation, the collected light would be formed purely from the unscattered, ballistic light. Practical imaging, however, is limited by the dynamic range of the detection scheme, which generally requires a higher signal level than that formed by a strictly ballistic signal. This means that above a certain (system dependent) optical depth threshold, the BI methods which strictly limit detection to the highest quality ballistic light are no longer viable.

Fortunately, the transmitted light is not a binary system made up of pure good (information carrying) and pure bad (noise) components. Ballistic light represents one end of a virtual continuum of photon classes each of which contribute to the signal representing the imaged object with varying degrees of fidelity. By slightly relaxing the light collection constraints to include "quasi-ballistic" light, a balance can be struck between the dynamic range of the detection optics, and the achievable spatial resolution of the imaging system.

Spatial filtering

Well collimated source light is discernibly spread by interaction with large particles in turbid media. Ballistic photons maintain their initial trajectories, while scattered photons, in aggregate, experience an angular spread according to the appropriate scattering phase function describing the photon-particle interactions. Papers VI and VII discuss this spreading effect in some detail, noting the dependence on the scattering phase function. This effect can be exploited to sort photons in a number of ways.

Fourier-plane filtering [63] attenuates specific spatial frequency components in an optical signal by blocking light near a focus. This can be realized in an optical system using a spatial filter consisting of matched lenses and a pinhole positioned at the plane of best focus. The focusing action of the first lens effectively transforms the signal field in spatial frequency space. The pinhole aperture attenuates high frequency spatial noise which appears at the periphery of the focal point, and the second lens reconstructs the light beam. Additionally, it is important to note that any optical train acts as a spatial filter, due to the finite acceptance angle of the optical components which make up the system. The severity of this spatial filtering can be enhanced or minimized based on the system geometry and individual components. Spatially limiting light collection can improve image contrast, but it is important to point out that this also limits or distorts the spatial bandwidth of the imaging system [28]. Consequently, one must consider

the trade-off between this contrast improvement and the necessary spatial resolution of the measured image. Fig. 3.2 shows the effect of spatial filtering on image contrast and intensity for imaging 2 lp/mm features through a solution of 0.7 μm polystyrene spheres at an optical depth of 5. The diagram of Fig. 3.3 shows this scattering arrangement and the collection acceptance angle limiting the light collection.

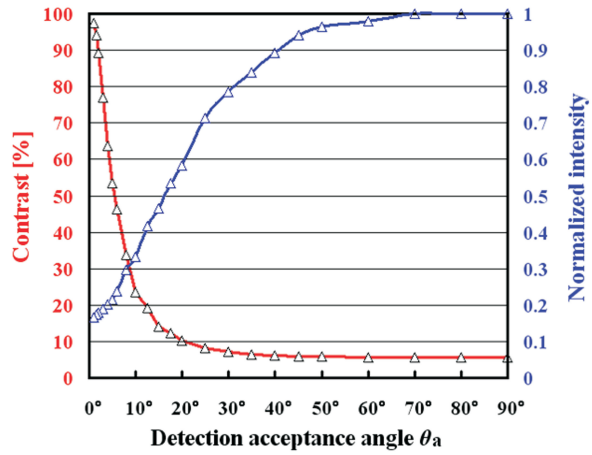

Figure 3.2: *Light collection acceptance angle; spatial filtering effects on image contrast for light scattered through 0.7 μm polystyrene spheres in water at optical depth 5.*

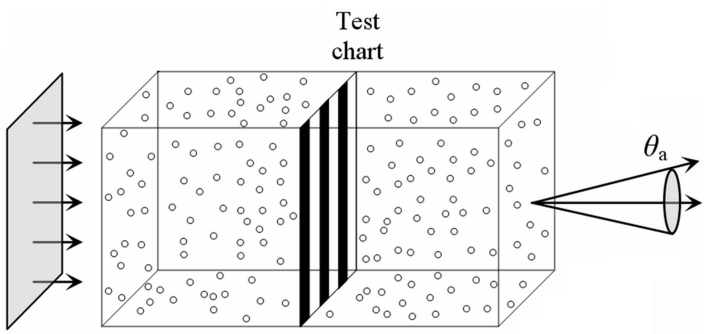

Figure 3.3: *Illustration of light scattering through a turbid medium and collected at a limited acceptance angle.*

Temporal filtering

When a beam of light interacts with scatterers in a turbid medium, most of the light is re-directed by scattering events, causing a temporal spreading of the incident light signal due to the differences in optical path length experienced by individual photons. Using source light in the form of a suitably short laser pulse results in a transmitted signal in which photons are sorted, with ballistic photons arriving first, followed by photons which have undergone more disturbing interaction with the scattering medium, resulting in greater differences in optical path length. Fig. 3.4 shows the effect of time-gating on image contrast and intensity for imaging 2 lp/mm features through a solution of 0.7 μm polystyrene spheres at an optical depth of 5. Fig. 3.5 shows a diagram of this scattering arrangement. Scattering media typical in the case of fuel sprays causes tem-

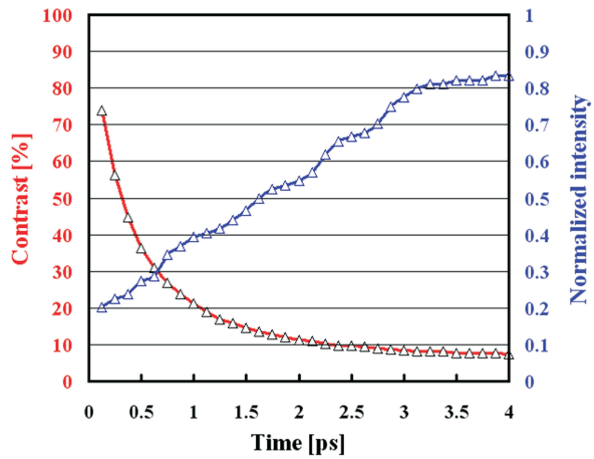

Figure 3.4: *Temporal filtering effects on image contrast for light scattered through 0.7 μm polystyrene spheres in water at optical depth 5.*

poral spreading on the order of picoseconds, so resolvable transmitted signals can be created using ~100 fs pulses attainable with commercially available mode-locked laser sources. The primary difficulty in temporal filtering is arranging detection of the photons in the leading edge of an optical signal on a picosecond time-scale, which is several orders of magnitude shorter than the speeds available using mechanical or electronic shuttering mechanisms.

A shutter which operates on picosecond or shorter timescales can be arranged by employing crossed polarizers in the image signal path which bracket a medium where a strong optical pulse induces a time-dependent anisotropy in the refractive index. If the strong (switching) pulse is spatially and temporally coincident with the leading edge of the imaging pulse, the resulting anisotropy causes a rotation of the polarization of the imaging pulse. This change in polarization results in time-dependent transmission through the second polarizer.

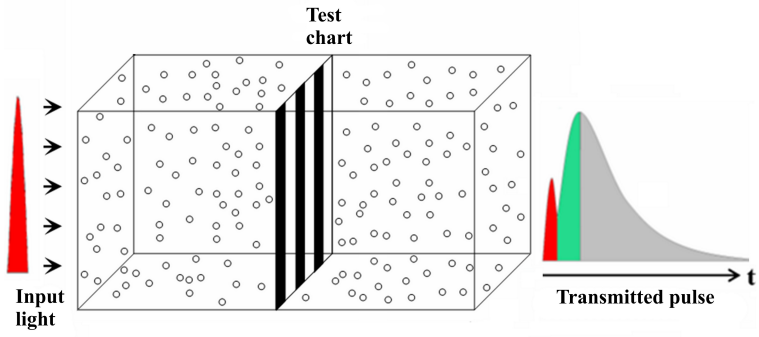

Figure 3.5: *Illustration of the temporal spreading of input light transmitted through a turbid medium due to path differences induced by scattering.*

The change in refractive index induced by an applied field is known as the optical Kerr effect (OKE). Following the notation and of Boyd [7], it is given by,

$$n = n_0 + 2\bar{n}_2|E(\omega')|^2 \tag{3.3}$$

which breaks the index of refraction into linear, n_0, and nonlinear, $\bar{n}_2$, components. This interaction arises from the material response of the medium to the strong field from the switching pulse and the weak field from the imaging pulse, in terms of the the nonlinear polarizability of the system (see Eq. 2.5).

The polarizability affecting the imaging beam at some frequency, ω' in the presence of a strong optical pulse at a frequency, ω, can be expressed as

$$P^{\text{Total}}(\omega) = \epsilon_0\chi^{(1)}E(\omega) + 6\epsilon_0\chi^{(3)}|E(\omega)|^2E(\omega') \tag{3.4}$$

where $\chi^{(1)}$ represents the linear susceptibility and $\chi^{(3)}$ is the third-order susceptibility. For convenience one can write the effective susceptibility,

$$\chi_{\text{eff}} = \chi^{(1)} + 6\epsilon_0\chi^{(3)}|E(\omega)|^2 \tag{3.5}$$

Recalling that

$$n^2 = 1 + \chi_{\text{eff}} \tag{3.6}$$

and substituting Eq. 3.3 for n on the left-hand side shows that the linear and nonlinear refractive indices can be written in terms of the linear and nonlinear susceptibilities, $\chi^{(1)}$ and $\chi^{(3)}$:

$$n_0 = \sqrt{1 + \chi^{(1)}} \tag{3.7}$$

and

$$\bar{n}_2 = \frac{3}{2}\frac{\chi^{(3)}}{n_0} \tag{3.8}$$

The Kerr effect can also be viewed as an intensity dependent response of the refractive index. Using Eq. 2.25, this gives

$$n = n_0 + n_2 I = 2n_0\epsilon_0 c|E(\omega)|^2 \tag{3.9}$$

Since this description must give the same result for the total refractive index, comparison with Eq. 3.3 yields the relation

$$n_2 = \frac{\bar{n}_2}{n_0\epsilon_0 c} \tag{3.10}$$

and from Eq. 3.8, n_2 is related to the third-order susceptibility, $\chi^{(3)}$ by:

$$n_2 = \frac{3}{2}\frac{\chi^{(3)}}{n_0^2\epsilon_0 c} \tag{3.11}$$

By introducing a polarized electric field with right and left circular polarization elements, and separating the non-linear polarizability into similar constituent polarization components, Eq. 2.10 can be solved in terms of an elliptically polarized wave. Here, the polarization of the transmitted wave will be rotated with respect to the input wave as a result of the nonlinear interaction, and the magnitude of the rotation will be proportional to the transit distance through the medium [7]. The diagram in Fig. 3.6 shows the OKE wavemixing process where the imaging beam, $E(\omega')$ experiences a birefringence in the Kerr medium caused by the response of the nonlinear susceptibility, $\chi^{(3)}$ and the switching beam, $E(\omega)$.

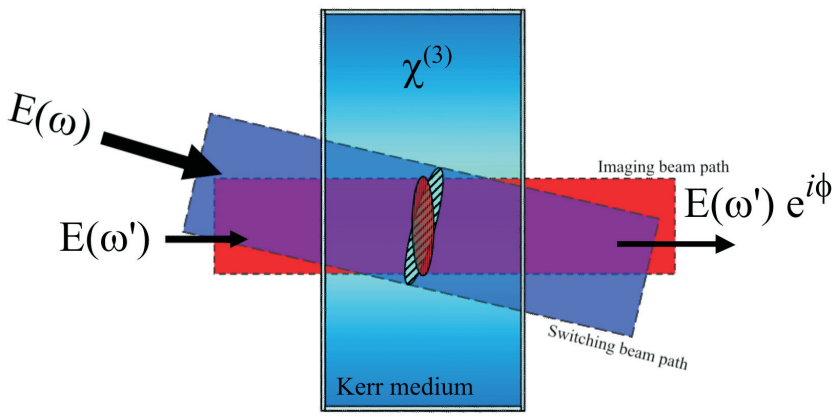

Figure 3.6: *Kerr effect wave mixing: the imaging beam, $E(\omega')$ experiences a birefringence in the medium caused by the response of the susceptibility, $\chi^{(3)}$ and the switching beam, $E(\omega)$.*

Various physical processes inherent to the medium where the Kerr effect is induced contribute to the nonlinear index of refraction, including: electronic hyperpolarizability, molecular orientation, electrostriction, saturated atomic absorption, and thermal effects. The third-order susceptibility, $\chi^{(3)}$, which describes the properties of the medium

in relation to the fields takes the form of a fourth-rank tensor and is therefore properly described by 81 individual matrix elements. Fortunately, most materials exhibit symmetries which greatly reduce the number of terms. For isotropic media in the presence of an arbitrary field, $\chi^{(3)}$ contains only three independent non-zero elements [29].

The OKE time-gate arrangement commonly used for BI consists of a glass cell filled with a transparent liquid which posesses a large value of n_2 and a short molecular relaxation time, τ_0. Typical choices are carbon-disulfide or nitrobenzene.

In this scheme, the dominant mechanisms behind the anisotropy of the refractive index are the electronic hyperpolarizability of the medium and the orientation effect of the liquid molecules [20]. The electronic effect can be represented by:

$$n_2^e = \frac{2\pi\rho}{3n_0}\gamma\left(\frac{n_0^2+2}{3}\right)^2\left(\frac{n_\omega^2+2}{3}\right)^2 \tag{3.12}$$

where ρ is the number density of the Kerr medium and n_ω is the linear index of refraction at the frequency ω. $\gamma = \frac{1}{5}\gamma_{iijj}^{\omega,\omega'}$ $(i,j=1,2,3)$ where $\gamma_{ijkl}^{\omega,\omega'}$ is a component of the fourth-rank tensor describing the electronic polarizability, at the angular frequency ω' of the imaging pulse, induced by the switching pulse at frequency ω.

Likewise, the orientation effect can be represented as:

$$n_2^o = \frac{2\pi\rho}{15kTn_0}\delta^2\left(\frac{n_0^2+2}{3}\right)^2\left(\frac{n_\omega^2+2}{3}\right)^2 \tag{3.13}$$

where k is the Boltzmann constant and T is the temperature of the medium in Kelvin. $\delta^2 = \frac{1}{4}(\alpha_{ii}^{\omega'} - \alpha_{jj}^{\omega'})\times(\alpha_{ii}^{\omega} - \alpha_{jj}^{\omega})(i,j=1,2,3)$ is a measure of anisotropy in the molecular polarizabilities $\alpha_{ij}^{\omega'}$ and α_{ij}^{ω} [51].

If the imaging beam is approximated by a Gaussian time and spatial profile,

$$\langle E_p^2(\omega', r, t)\rangle = \frac{1}{2}E_0 e^{-(t^2/\tau_p^2)}e^{-(r^2/r_p^2)} \tag{3.14}$$

where τ_p is the pulse duration and r_p is the beam radius, the birefringence is given by

$$\Delta n = n_2^e\langle E^2(t)\rangle + n_2^o\, E_p^2\,\frac{\tau_p}{\tau_o}\,\sqrt{\pi}\,\mathrm{erf}\left[\sqrt{2}\left(\frac{t}{\tau_p} - \frac{\tau_p}{2\tau_o}\right)\right]\times\exp\left[\frac{\tau_p^2}{4\tau_o^2} - \frac{t}{2\tau_o}\right] \tag{3.15}$$

where τ_o is the molecular reorientation time characteristic to the medium. The total phase shift experienced by the imaging beam over a distance, ℓ, is then

$$\Delta\phi(t) = \frac{2\pi}{\lambda}\ell\Delta n \tag{3.16}$$

and the transmitted intensity for the medium arranged between crossed polarizers is given by

$$I = I_0\sin^2(\frac{\Delta\phi}{2})\sin^2(2\theta) \tag{3.17}$$

where θ is the angle between the polarization vectors of the switching and imaging beams. For a Kerr cell filled with carbon-disulfide and gated with a 100 fs pulse, typical gating times are less than 2 ps, with transmission efficiencies of 50% or more [24]. Fig. 3.7 shows calculated and measured transmission values for a carbon-disulfide OKE time-gate arrangement.

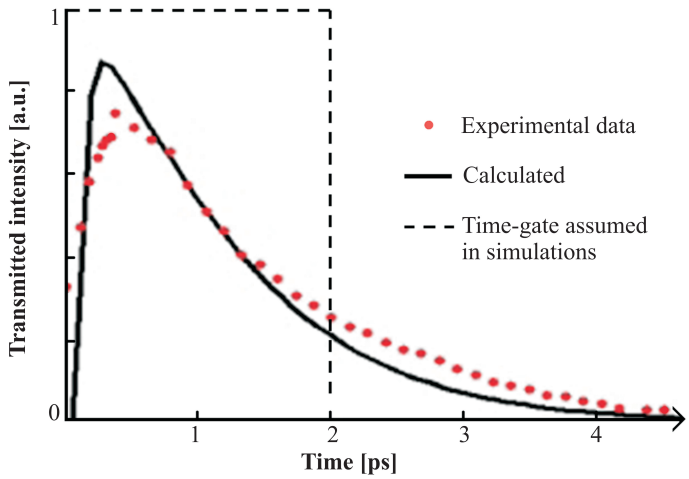

Figure 3.7: *Kerr effect time-gate transmission as a function of time.*

Polarization filtering

The detailed polarization effects induced by interactions in a turbid medium depend very much on the specifics of the scatterers and the symmetry of the system. This topic is discussed at length by Van de Hulst (Ch.4–5) [60]. For spherical particles in a homogenous distribution, strict forward scattering (scattering angle zero) has absolutely no effect on the polarization. In most cases, it is reasonable to assume that ballistic and quasi-ballistic photons maintain their initial polarization while the medium imparts random polarization to photons which are involved in many scattering interactions. This allows a portion of the diffuse light signal to be suppressed directly through an appropriate arrangement of the polarization of the source light and polarizers in the collection optics.

Coherence filtering

Well-formed source light produced by laser oscillators exhibits a high degree of coherence. The phase of individual photons is altered by scattering interactions in turbid media. This changes the relative phase, and therefore coherence, with the input light. By arranging a detection scheme that relies on coherent interference of the source and

scattered light to generate a signal, coherence properties can be used to discriminate photons for BI.

A large number of arrangements are possible, including: interferometric techniques and holography [8, 48, 53], second-harmonic generation [65], sum- or difference-frequency generation, coherent anti-Stokes Raman scattering, parametric amplification [64], and stimulated Raman scattering [3, 13]. Coherence gating techniques can be quite effective, however photons are quickly dephased by scattering interactions, which means that coherence gating strictly limits detection to only the highest quality ballistic light. This represents a serious drawback for imaging in highly turbid media, since the coherent signal available for imaging can easily fall below detection limits for the system.

Chapter 4

Ballistic imaging in sprays

The fluid dynamics of atomizing sprays involve a complicated interaction of fluid properties, forces, mixing, and energy transfer which is not fully understood[30]. For many sprays, complete characterization of the flow is problematic due, first, to the sensitivity of the flow which renders probes or devices placed in the flow volume impractical, and second, to the high turbidity of some regions of the flow, often termed the near-field or dense spray regions. These dense portions of the spray frustrate most optical diagnostics due to the large amounts of distortion and attenuation caused by scattering in these regions.

4.1 Two-phase jet-in-crossflow

This section discusses experimental work in which the time-gated BI instrument designed by Paciaroni and Linne [47] was applied to a water jet issuing into a crossflow of air. Paper II presents analysis of the spray images obtained in these measurements and discusses the flow regimes covered by the test conditions, noting unusual behavior, including possible bifurcation of the liquid flow under some conditions. Table 4.1 lists the run conditions examined in this work.

The apparatus used to generate the water spray and direct the crossflow of air was designed in collaboration with the Large Eddy Simulation modelers at Lund University to enable the investigation of jet-in-crossflow conditions with well-established boundary conditions. The test section consists of a low-turbulence spray nozzle mounted in a channel with a square, 80 x 80 mm cross section, constructed of aluminum profile, with a length of 3.1 m. Five optical glass windows, mounted flush with the inside wall of the channel, provide access for imaging the spray.

The BI instrument used in these experiments is depicted in Fig. 4.1. The optics and system layout were optimized by Paciaroni using OSLO, a commercial optics code [47]. The design is assembled from commercially available components, arranged in an optical train which minimizes aberrations and distortions of the light signal, resulting in a diffraction limited imaging system.

Table 4.1: *Jet-in-crossflow run conditions.*

We	Case	d_j (mm)	U_j (m/s)	U_g (m/s)	Re_j	q
21	9	0.5	10.4	48	5.18×10^6	37
21	2	0.5	21	48	1.05×10^7	153
29	4	0.7	21	48	1.46×10^7	153
34	8	0.5	13.5	62	6.72×10^6	38
40	7	0.5	15	67	7.47×10^6	40
41	6	1	21	48	2.09×10^7	153
49	1	0.5	21	74	1.05×10^7	64
68	3	0.7	21	74	1.46×10^7	64
98	5	1	21	74	2.09×10^7	64
122	10	1.25	21	74	2.61×10^7	64

A 1 kHz repetition rate Ti:Sapphire regenerative amplifier (Spectra-Physics Spitfire), seeded with a mode-locked Ti:Sapphire oscillator (Spectra-Physics Tsunami) was used to generate 1 mJ pulses with a pulse duration of 80 fs, centered in wavelength at 800 nm. The linearly polarized pulse produced by the amplifier was divided by a 70/30 beamsplitter (Melles-Griot 03BTF021) into switching and imaging beams.

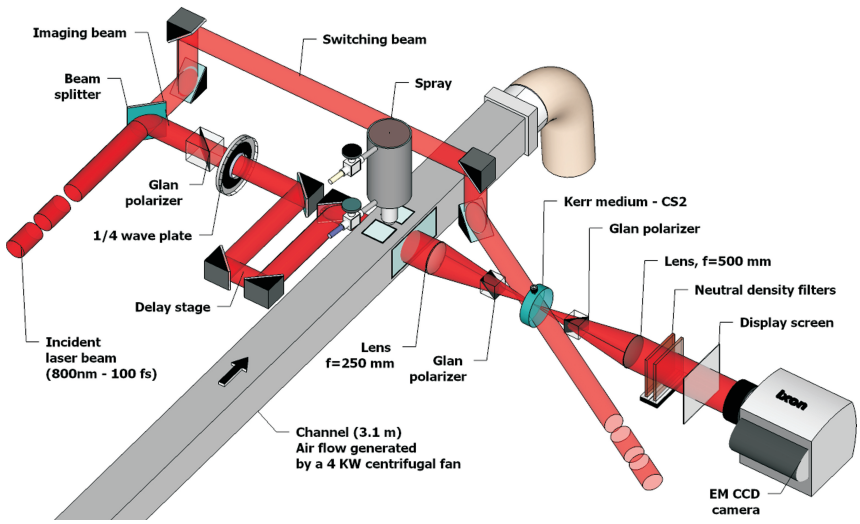

Figure 4.1: *BI experimental arrangement for near field imaging of the jet-in-crossflow.*

The switching beam was directed by four turning mirrors (Edmund Scientific 45597) through a glass cuvette filled with carbon-disulfide, where it crosses the path of the imaging beam at a shallow angle, $\sim 14°$. The liquid filled cuvette has an optical path

length of 1 cm, and serves as a Kerr medium, providing a time-dependent birefringence controlled by the switching beam energy (Sec. 3.3).

The imaging beam was time delayed using an arrangement of turning mirrors on a delay stage. This allowed the length of the imaging beam path to be adjusted to control the temporal overlap between the switching and imaging pulses at the point where they cross in the Kerr medium. Following the time-delay the imaging beam was directed through a Glan-polarizer (25 mm clear aperture), ensuring linear polarization, and a waveplate, which rotates the polarization by 45° to provide the appropriate polarization state to maximize transmission through the Kerr medium. The imaging beam was then directed through the spray and collected by a lens (Newport PAC088, $f = 250$ mm) placed one focal distance from the center of the spray. Light collected by the lens was focused through the OKE shutter, consisting of crossed Glan-polarizers which bracket the Kerr medium. Light transmitted by the OKE shutter was subsequently collected by a second lens (Newport PAC091, $f = 500$ mm) and directed to a display screen where it was imaged by an EM-CCD camera (Andor iXon DU-897).

The BI instrument described here eliminates a large percentage of the forward-scattered source light transmitted by the spray based on its collimation, polarization, and optical path length. This light collection arrangement is termed a source projection scheme, in reference to the action of the first lens, which is placed one focal distance from the plane of interest. This placement changes the efficiency of the light collection from the object plane. This results in a spatial filtering effect in which the collection of uncollimated light scattered behind the object plane is reduced, while the collection of well-collimated light remains unaffected. This is similar to the arrangement of a condenser lens used to project light from a small source into an optical system. The length of the system and apertures of the system components also contribute a spatial filtering effect. Light which is depolarized by scattering within the spray is attenuated by the first polarizer. The remainder of the light pulse which has propagated to the Kerr medium is subjected to a time-dependent birefringence, resulting in a time-gating effect allowing full transmission of this light through the second polarizer during a short, ∼2 ps, time window.

The projection light collection scheme increases collimated light intensity from the object plane, resulting in increased contrast, especially at low spatial frequencies. The transmitted intensity field is a projection, however, and not an image plane with a conjugate relationship to the object. This is apparent from the measurement results, since even features in areas of low turbidity appear as shadowy regions, lacking the detailed spatial frequency information of a focused image. Two examples of a time-gated ballistic images produced by this instrument are shown in Figs. 4.2 and 4.3.

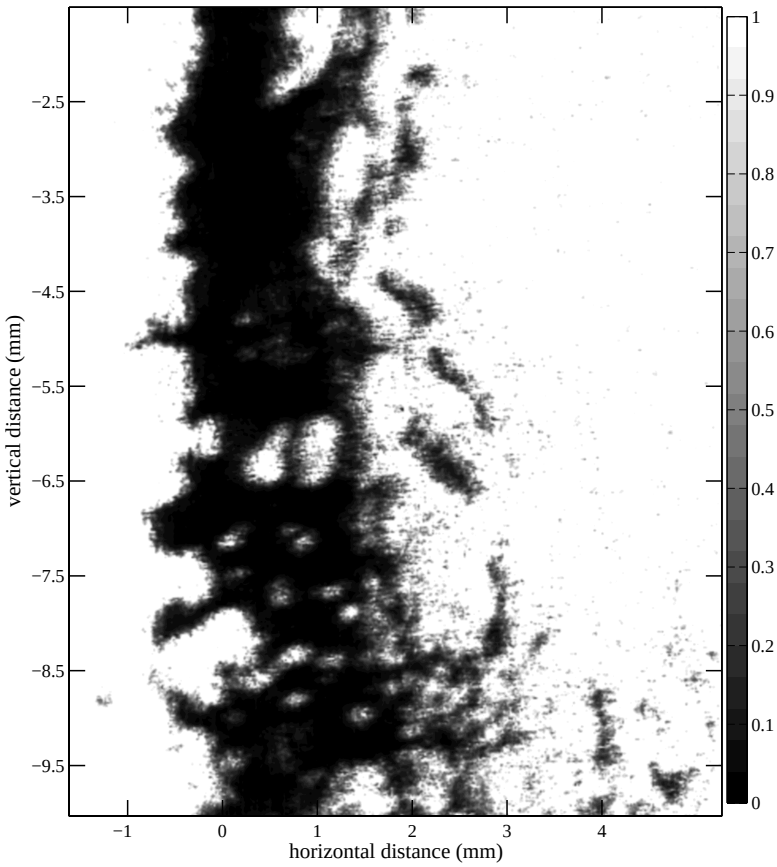

Figure 4.2: *Time-gated ballistic image of a water jet issuing downward into a crossflow of air incident from the left. Case 1 conditions ($We = 49$), as indicated in Table 4.1.*

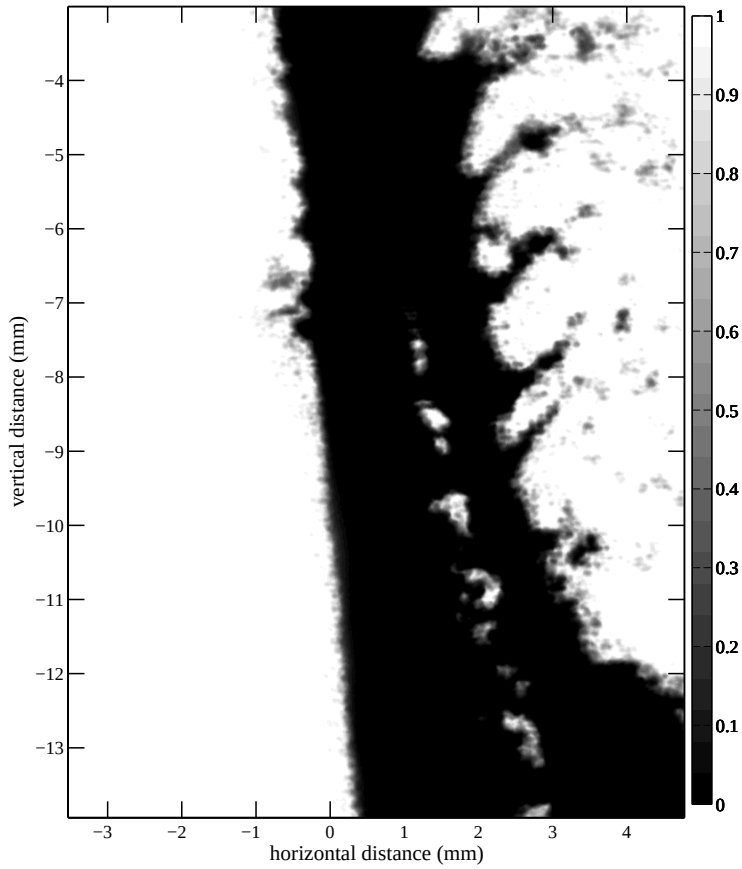

Figure 4.3: *Time-gated ballistic image of a water jet issuing downward into a crossflow of air incident from the left. Case 3 conditions (We = 68), as indicated in Table 4.1.*

4.2 Aerated spray

A time-gated BI instrument designed for transient fuel sprays measurements was applied to an effervescent spray [55] issuing into ambient air. Preliminary results from these measurements are mentioned in Paper I. Paper III gives a brief introduction to effervescent sprays, and presents analysis of images obtained in this campaign which highlight the influence of flowrate on the breakup of aerated sprays. Paper V presents velocity analysis of images generated by this work.

The spray studied here was a water jet, issuing into quiescent air at atmospheric pressure, generated by the Portable Barbotage Injection Rig (PBIR). This system was designed by the Propulsion Directorate at the Air Force Research Laboratory to study aerated spray effects relevant to scramjet operation using liquid hydrocarbon fuels. The system is supplied by a nitrogen-pressurized water reservoir and bottled nitrogen. The liquid and gas flows are controlled by a set of 4 choke valves and continuously measured by a bank of turbine mass flowmeters and sonic nozzles, respectively.

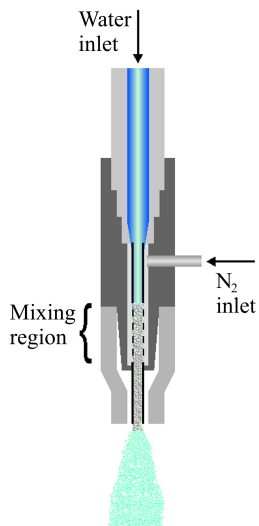

Figure 4.4: *Diagram of the effervescent spray nozzle.*

The system supplies separate flows of liquid water and nitrogen gas to a specially constructed nozzle (see Fig. 4.4). Here, the liquid flows down through a 1.3 mm central tube while nitrogen gas, at a slightly higher pressure, flows through an annular region surrounding the central tube. At the mixing region, the wall of the center tube is perforated by 178μm holes, allowing the liquid and gas to mix. This arrangement rapidly merges the liquid and gas flows at elevated pressures ($\sim$1.14 MPa), at which point the flow proceeds to the nozzle outlet. The system can be run with a 0.5 mm and a 1 mm diameter nozzle orifices, each with a length-to-diameter ratio of 20.

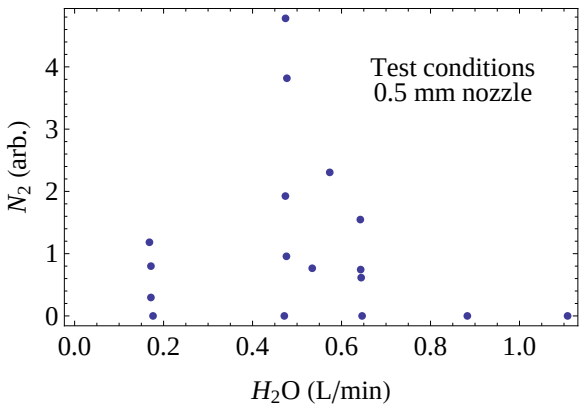

Re_ℓ	Q_L (L/min)	GLR
9k	0.18	0.00
9k	0.17	1.73
9k	0.17	4.66
9k	0.17	7.03
25k	0.47	0.00
25k	0.48	2.01
25k	0.47	4.10
25k	0.48	8.00
28k	0.53	1.43
34k	0.65	0.00
34k	0.64	1.16
34k	0.64	2.41
54k	1.11	0.00

Figure 4.5: *Effervescent spray run conditions for the 0.5 mm nozzle.*

Effervescent sprays exhibit unique behavior due to the structure and multiphase nature of the flow inside the nozzle, and breakup is known to be a strong function of the gas-to-liquid ratio (GLR). A wide range of conditions were investigated in this study, essentially covering the parameter space for stable operation of the PBIR. The system conditions for the 0.5 mm nozzle are shown in Fig. 4.5 and the conditions for the 1 mm nozzle are detailed in Fig. 4.6.

The BI system used in these measurements was designed to discriminate light in a manner similar to the instrument discussed in Sec.4.1 using a simplified optical arrangement. Input light for the system was provided by a specialized ultrafast laser system capable of generating two pulses with a selectable time separation, at a repetition rate of 1 kHz. The source consists of a single mode-locked Ti:Sapphire oscillator (Vitesse) which seeds two regenerative amplifiers (Libra), each pumped by an independent Q-switched Nd:YLF laser (Evolution). The output of both regenerative amplifiers is combined in a single beam, with adjustable inter-pulse spacing controlled by the pump laser timing. Dual pulses with 1 mJ of energy and a pulse width of 100 fs were used to obtain time-resolved image pairs of the aerated spray with a time-separation of 10 μs.

A diagram of the optics used to direct source light to the spray and to subsequently collect and discriminate light for detection is shown in Fig. 4.7. In this configuration, source light is directed through a waveplate in a rotation mount, which partitions the source intensity in vertical and horizontal linear polarizations. A polarizing beamsplitter divides the source pulse into "imaging" and "switching" pulses, containing roughly 30% and 70% of the incident beam energy, respectively.

The imaging light advances from the beamsplitter through a polarizer and waveplate, and is expanded in a 1:4 telescope, before crossing the measurement volume where it interacts with the aerated spray to generate the scattered signal. Forward-scatter light

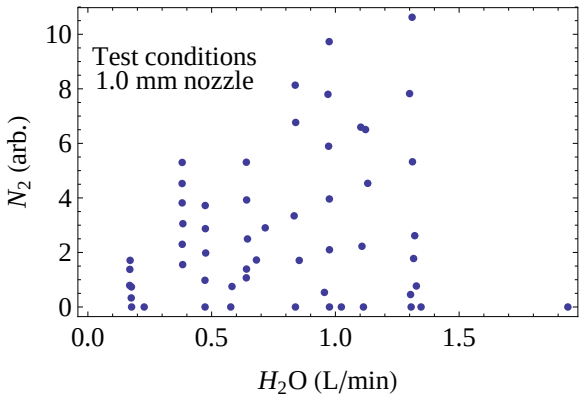

Re_ℓ	Q_L (L/min)	GLR
4.5k	0.18	0.00
4.5k	0.18	1.90
4.5k	0.17	4.68
4.5k	0.17	10.0
12.5k	0.47	0.00
12.5k	0.47	2.07
12.5k	0.48	4.16
12.5k	0.47	7.85
26k	0.98	0.00
26k	0.98	2.15
26k	0.98	4.06
26k	0.97	8.04
29k	1.11	0.00
29k	1.11	2.01
29k	1.13	4.01
29k	1.10	5.98

Figure 4.6: *Effervescent spray run conditions for the 1 mm nozzle.*

from the spray is collected by a plano-convex lens ($f = 500$ mm) with a collection aperture defined by the alignment of two mirrors. The collected light is focused through the Kerr effect shutter which consists of crossed polarizers bracketing an optical glass cell filled with a carbon-disulfide.

The switching pulse is directed from the beamsplitter through a waveplate and to the Kerr medium by reflective optics, which include a path length adjustment stage. The switching light is directed along a precisely defined course, such that the optical path length traversed by the switching pulse is matched to the optical path length of the imaging pulse at the Kerr medium. A fast-framing detector (Phantom 7) is placed at the imaging distance ($\sim 2f$) of the collection lens to capture the image.

The BI instrument described here eliminates most of the forward-scattered light transmitted by the spray in largely the same fashion as the system discussed in Sec. 4.1. The spatial filtering of the optical arrangement segregates light based on its degree of collimation, polarization optics filter out light which is randomly polarized by the spray, and the Kerr-effect shutter attenuates all light excepting that which reaches the Kerr medium within a $\sim$2 ps time window, essentially sorting light based on its optical path length through the medium.

The key difference is the light collection arrangement, which uses a single lens placed at twice the focal distance from the object plane and a detector placed at twice the focal distance from the collection lens. The arrangement is termed a source imaging scheme, in reference to the light collection of the first lens, which matches the familiar condition for imaging with unit magnification. The light collected by the lens forms an

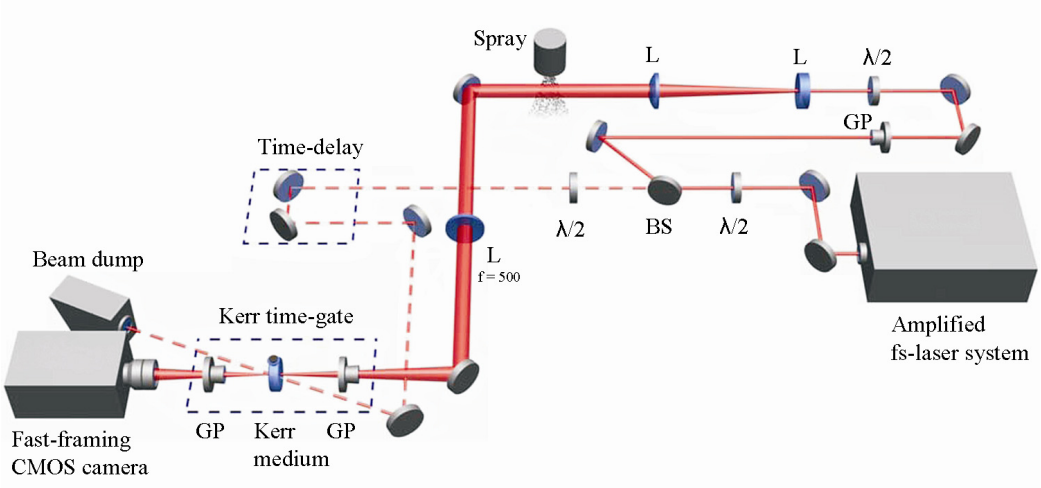

Figure 4.7: *BI experimental arrangement for near field imaging of the effervescent spray.*

image with a conjugate relation to the object plane directly on the light-sensitive CMOS array. This light collection scheme preserves high frequency spatial information from the object plane, but reduces the light contributed by each point in the object plane, since the irradiance filling the aperture of the lens decreases according to the inverse square of the distance to the object plane. Time-gated ballistic images produced by this arrangement are shown in Figs. 4.8-4.10.

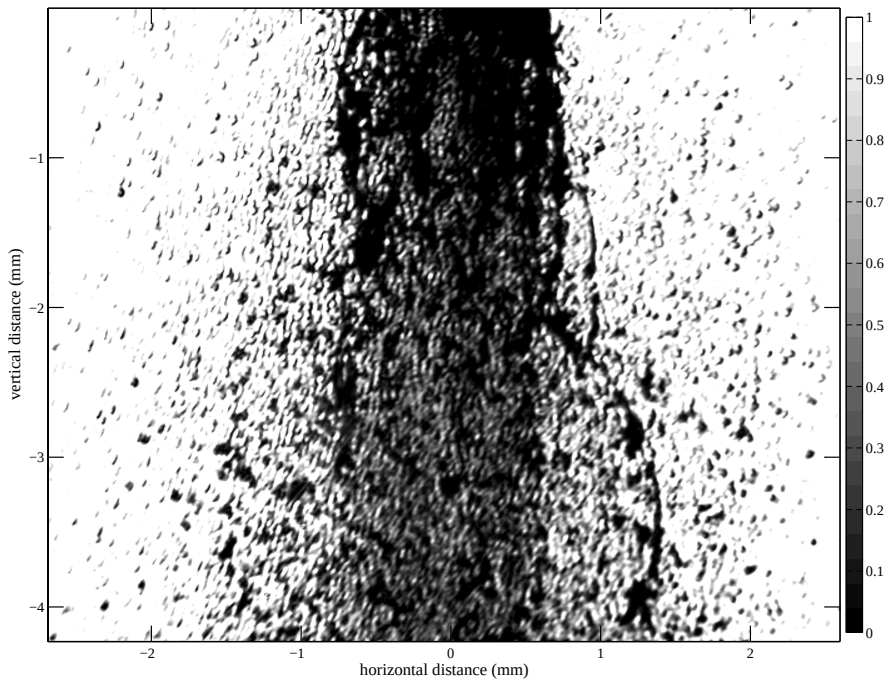

Figure 4.8: *Time-gated ballistic image of aerated spray. GLR* $= 2.24$*,* $Q_L = 0.82$ *L/min.*

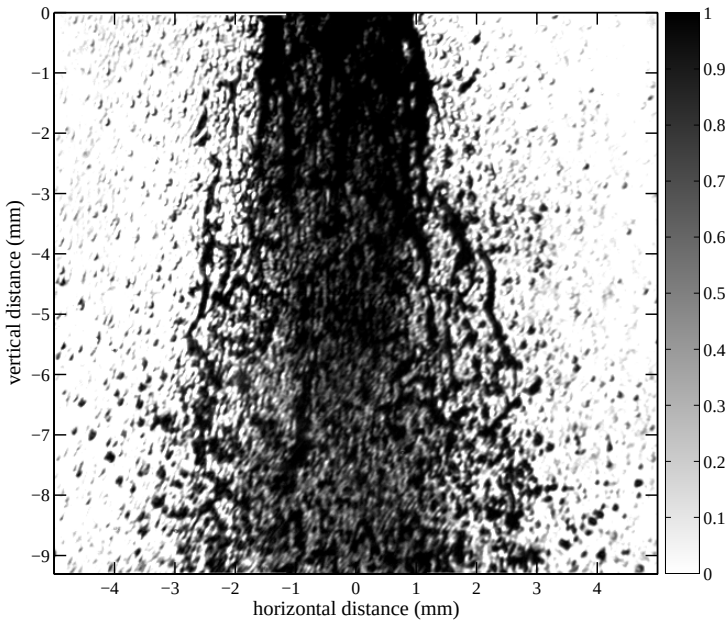

Figure 4.9: *Time-gated ballistic image of aerated spray. GLR* $= 1.99$*,* $Q_L = 0.67$ *L/min.*

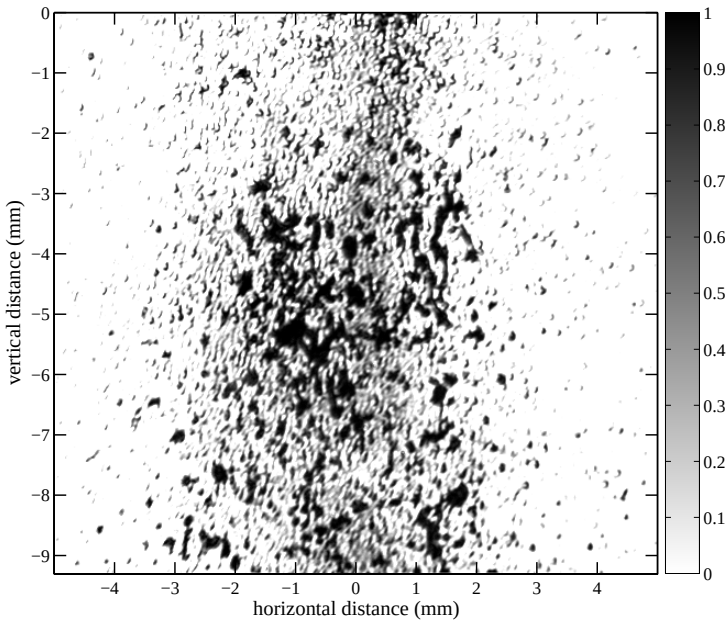

Figure 4.10: *Time-gated ballistic image of aerated spray.* $GLR = 10$, $Q_L = 0.78$ *L/min.*

4.3 Spray velocity

Both of the BI systems discussed in the preceeding sections (Sec. 4.1 & 4.2) were applied in double-image configurations with the aim of determining velocity vectors from the resulting spatial intensity information.

The system shown in Fig. 4.1 was adapted for velocity imaging by shutting off the crossflow air and slowing the liquid flow until a steady sequence of falling droplets was generated. This setup enabled the 1 kHz BI system to capture successive images of falling drops. Pairs of high-resolution ballistic images were recorded using an interline transfer CCD (Princeton PI-Max) with a time separation of 1 ms. Paper IV discusses the feasibility of measuring velocity in a spray from successive ballistic images, and presents velocity results determined from a set of these images as a proof-of-concept for the larger task of extracting velocities from a dense field of droplets.

The BI system used to study the aerated spray (shown in Fig. 4.7) utilized a laser source capable of generating two ultrafast light pulses with a user-selected time separation, at repetition rate of 1 kHz. Using this system, pairs of ballistic images of the aerated spray were acquired with a temporal separation of 10 μs using a fast-framing CMOS camera (Phantom 7.0). Paper V successfully demonstrates the efficacy of velocity analysis in a dense spray using these images and presents a targeted correlation method that improves the accuracy and data rate for velocity determination in dense regions of the flowfield.

Velocity analysis

The determination of velocity information from a series of images is based on the concept of "optical flow," which is given by the apparent motion of the spatial intensity between corresponding frames in a sequence of images. For intensity normalized images with a short time separation, the local image intensity can be assumed to be constant. Given a distinct region of a spatial intensity pattern that is displaced from one image to the next, over a time, Δt and a distance, $\{\Delta x, \Delta y\}$, the intensity of the region (assumed constant) can be written as

$$I(x, y, t) = I(x + \Delta x, y + \Delta y, t + \Delta t) \tag{4.1}$$

Expanding this description in a Taylor series about the point (x, y, t) yields the expression

$$I(x, y, t) = I(x, y, t) + \Delta x \frac{\partial I}{\partial x} \Delta y \frac{\partial I}{\partial y} + \Delta t \frac{\partial I}{\partial t} + \epsilon \tag{4.2}$$

where the higher order terms in Δx, Δy, and Δt are written into ϵ. Subtracting $I(x, y, t)$ and dividing through by Δt gives

$$\frac{\Delta x}{\Delta t} \frac{\partial I}{\partial x} + \frac{\Delta y}{\Delta t} \frac{\partial I}{\partial y} + \frac{\partial I}{\partial x} + \vartheta(\Delta t) \tag{4.3}$$

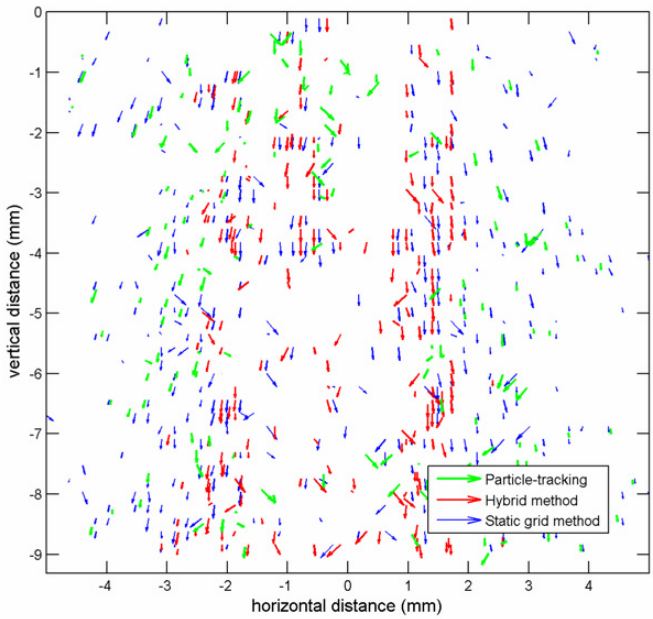

Figure 4.11: *Velocity vectors for aerated spray, GLR = 10%. The t_1 image used in this analysis is shown in Fig. 4.10*

where $\vartheta(\Delta t)$ is a term of order Δt. In the limit as $\Delta t \to 0$, this leads to the equation for optical flow[22]:

$$\frac{\partial I}{\partial x}\frac{dx}{dt} + \frac{\partial I}{\partial y}\frac{dy}{dt} + \frac{\partial I}{\partial t} \approx 0 \tag{4.4}$$

where $\frac{dx}{dt}$ and $\frac{dy}{dt}$ are the components of the motion to be estimated from a pair of images in a sequence. This equation relates the change in spatial intensity at a point to the motion of the spatial intensity pattern. This is simply a formal statement of what one intuitively expects from a clear image of a scene. Namely, that the apparent motion of things in the scene reflect the actual motion of those things and not some fluctuation in the base intensity.

A variety of approaches have been developed to solve for the motion of spatial intensity patterns in successive images[38, 57]. The methods developed as part of this work for analysis of ballistic images are based on region-matching, utilizing normalized cross-correlation of strategically defined subregions from corresponding image pairs.

Prior to analysis, the images are divided by an adjusted image background which is formed by a morphological opening followed by a gaussian smoothing of the measured background. This adjustment eliminates small scale structures caused by laser speckle in the measured background and eliminates any partially resolved structure in the image

resulting from objects which are only slightly smaller than the spatial resolution of the system.

Velocities are determined from a set of square image regions, which are selected from the t_1 image and cross-correlated with a set of square regions from the t_2 image. Peaks in the cross-correlations indicate displacements for the selected regions, yielding x and y velocity components as shown in Eqn. 4.4.

Dense sprays present challenging spatial intensity variations for correlation analysis, including large variations in structure throughout the field of view. Small, well-separated droplets appear on the spray periphery, while interior of the spray includes distributed liquid structures and voids with varying amounts of contrast (see Fig. 4.10). To acquire more velocity information throughout the spray and to increase the accuracy of the cross-correlation matching, four different selection methods were implemented to choose the image regions used to calculate velocity:

- edge targeting
- conventional grid analysis (Grid)
- particle-tracking (PT)
- image segmentation with subsequent grid analysis (Hybrid)

Edge targeting is implemented by applying Sobel edge detection to center correlation windows on strong gradients in the images which indicate liquid-gas boundaries. In situations where structures can be positively matched in an image pair, the bulk motion of the structures can be separated from the total motion of the edge, allowing the small-scale motion of the liquid-gas boundary to be tracked. Paper IV demonstrates analysis based on this method to track the deformation of a falling droplet. Conventional grid analysis is the standard untargeted approach implemented by segmenting the entire field-of-view with a regular grid for correlation analysis. Particle-tracking is implemented using thresholding [44] and image segmentation [50]. This method can be applied to obtain velocity for small droplets resolved in the images. Image segmentation with subsequent grid correlation analysis is a targeting method applied over the resolved fluid features larger than a reasonable size threshold for droplets. This method is implemented by identifying regions with thresholding and image segmentation, and subdividing these regions for correlation analysis.

Error estimate

To understand the capabilities offered by the targeting methods discussed in Sec. 4.3, it would be useful to examine a known, less complicated flow as a reference. However, since the morphology of the individual liquid features is a determining parameter in the calculation of the flow velocity, generating a random image of droplets with appropriate sizes and concentrations which permit the targeting approaches to be evaluated is not trivial. One can readily envision analysis of artificially generated images which

oscillates between poor and perfect performance, based on the morphology chosen for the artificial droplets and the geometry of their placement.

To avoid this difficulty, the targeting approaches were tested using ballistic image data from a real spray, where a second "artificial" image was generated by translating the image data by a known offset. This allowed application of velocity analysis to recover the known offset and errors in the analysis as spurious correlation vectors.

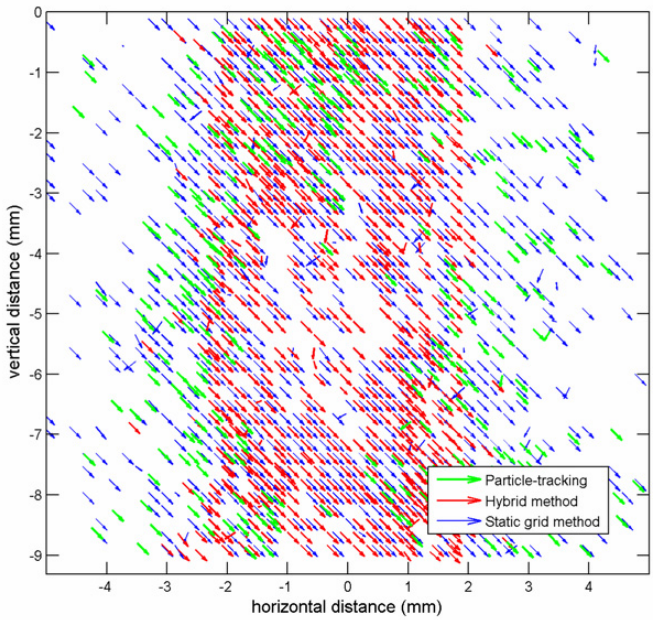

Figure 4.12: *Known velocity field test, 60% correlation strength validation.*

Figs. 4.12 and 4.13 show the results of this test. In most cases, the offset is correctly deduced by the correlations. However, one can observe isolated individual vectors, in all three approaches, where the correlation produces a peak that does not reflect the offset. This is a consequence of the specific morphology of the features chosen for correlation and the context of these features in the spatial intensity field. Irregular (brighter) illumination in some areas of the image can also lead to erroneously placed maximum correlation values.

The grid approach is the worst offender in this regard, since the window selection for the grid vectors is based on regular division of the entire image, and not guided by any aspect of the spatial intensity field. The performance of the targeting approaches is very dependent on the details of the flow, but the window selections which are guided by connectivity of the liquid phase appear to serve their intended purpose: they result in a more uniformly distributed velocity field and more vectors which pass the vali-

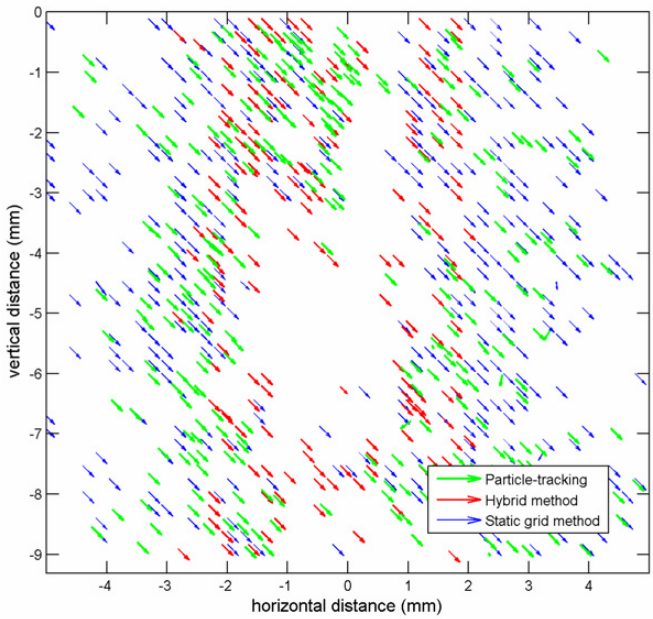

Figure 4.13: *Known velocity field test, 90% correlation strength validation.*

dation criteria. Additionally, applying the targeting based on connectivity appears to marginally reduce the occurrence of spurious correlations.

The vectors are first validated by an autocorrelation check, where the selected base image region is correlated with a search field taken from the base image itself. Regions that return non-zero autocorrelation vectors are discarded. The vectors are further validated by correlation strength. This is a somewhat sensitive parameter, given that one sacrifices good velocity information as this parameter is made more stringent.

Table 4.4: *Velocity correlation errors for targeting methods discussed in Sec. 4.3.*

corr.	PT	Hybrid	Grid
60%	3/313	23/713	42/928
(Fig. 4.12)	< 1%	$\sim$ 3%	$\sim$ 4.5%
95%	3/279	0/109	4/327
(Fig. 4.13)	$\sim$ 1%	0%	$\sim$ 1%

Figs. 4.12 and 4.13 are made with two different correlation strength validation parameters to clarify the trade-off between total accuracy and the amount of velocity information available when adjusting this parameter. Fig. 4.12 is calculated with 60%

correlation required to validate a vector, while the image shown in Fig. 4.13 requires 95%. The errors for both figures are listed in Table 4.4.

Chapter 5

Ballistic imaging system model

The ballistic imaging system model is a set of programs that work together to define a scattering volume, instrument optics and a light source. The intense short pulse source light is modeled by numerous photon packets which are transmitted through the scattering volume and optics to form a spatial intensity profile at the output plane. The system model allows quantitative evaluation of different imaging instruments and light filtering schemes. This provides the opportunity to optimize individual components, identify problems in current systems, and test the feasibility of new measurement objects, light sources, or optical designs. Papers VI, VII, and VIII present analysis of light scattering results obtained from this model, which was developed over the course of the present work.

The system model incorporates a validated Monte Carlo code for light scattering in random inhomogenous media coupled to a ray-tracing model which treats the full optical system. The modeling approach for the description of light in the Monte Carlo code is briefly discussed in the next section. This code was initially developed by Berrocal and Meglinski, and full details concerning it's design and implementation are detailed in the thesis by Berrocal [4].

5.1 Light propagation: Monte-Carlo

The irradiance, given in Eq. 2.25, defined the amount of light incident on a surface by tracking the average energy per unit area per unit time. By defining a volume element representing an infinitesimal volume in the scattering medium, we can use a similar quantity, the radiance (irradiance per unit solid angle), to track the average energy leaving and entering this volume.

The optical properties of the volume element are assumed to be homogenous, such that the interactions of photons and scatterers within the element are statistically averaged and interactions within the volume are assumed to be mutually independent. This requires that the wavelength of the incident radiation is small compared to the scattering medium. For most turbid media, where optical disturbances are caused by

interactions with large independent particles, these are valid assumptions.

On these terms, the propagation of a light pulse in turbid media can be described by the equation of radiative transfer (ERT):

$$\frac{1}{c}\frac{\partial L(r,s',t)}{\partial t} = -\mu_s L(r,s',t) - \mu_a L(r,s',t) + \mu_s \int_{4\pi} f(s',s)L(r,s,t)d\Omega' \qquad (5.1)$$

where r represents the position vector, s is a unit vector in the direction of the incident radiance, t is time, c is the speed of light, and L is the radiance in units of W/Sr·cm^2. The ERT expresses how the change of radiance along a line of sight corresponds to the loss of radiance due to the extinction of the incident light, plus the amount of radiance that is scattered back into the incident direction from all other directions. In general, it is not possible to solve the ERT analytically without resorting to simplifying assumptions that severely limit it's application [25]. Fortunately, stochastic approaches are available that allow numerical solutions which are equivalent to solving the ERT. One such approach is the Monte Carlo method.

The Monte Carlo approach relies on repeated random sampling of one or several probability distributions that accurately portray the possible values of a quantity to be determined. Individually, each randomly determined answer represents only a possible answer. Large numbers of randomly determined values in aggregate, however, begin to portray the exact value, as represented by the probability distributions. Provided a statistically significant number of samples can be evaluated, the investigated quantity can be accurately calculated.

The Monte Carlo method is applied to light propagation in turbid media by stochastically modeling light as a photon packet representing a group of photons which take a similar statistically averaged path through the medium.

Each photon packet is launched from the light source with predefined properties appropriate for the source light, including it's overall angular and spatial distribution. Each photon packet propagates according to it's initial properties until it encounters an interaction. The distance traveled before an encounter is determined by randomly sampling the free path length, l_{fp}, from the probability for a photon to be scattered or absorbed

$$P(l_{\text{fp}}) = \mu_e e^{-\mu_e l_{\text{fp}}} \qquad (5.2)$$

Sampling this distribution with a uniform random number, ξ, distributed over the interval 0 to 1, yields

$$l_{\text{fp}} = -\frac{\ln \xi}{\mu_e} \qquad (5.3)$$

The nature of the photon packet interaction at each encounter is randomly determined from the probability of a photon to be absorbed or scattered at an interaction, which is given directly by the albedo,

$$\text{A} = \frac{\mu_s}{\mu_s + \mu_a} = \frac{\sigma_s}{\sigma_e} \qquad (5.4)$$

As the ratio of the scattering and extinction coefficients, the value of the albedo naturally lies between 0 and 1. A new random number is generated to sample this distribution, such that

$$\begin{array}{ll} \xi > A, & \text{absorption occurs} \\ \xi < A, & \text{scattering occurs} \end{array} \tag{5.5}$$

If absorption occurs, the photon packet ends it's journey. If scattering occurs, the properties of the photon packet are adjusted and the next encounter is calculated.

When scattering occurs, the new propagation direction must be sampled from a probability formed according to the angle of incidence of the photon packet, and the Mie theory scattering phase function. This is implemented, first, by defining the direction s, and the angles Φ and Θ, of the photon packet before the scattering event, according to the global coordinate system (X,Y,Z). The system is transformed into a local coordinate system for the photon packet (U, V, W), where the direction of propagation is aligned with W axis. With this formalism the polar and azimuthal angles, Θ_s and Φ_s, defining the direction after scattering can be sampled from the cummulative probability density function computed from the phase function for the scattering interaction. With the new direction defined, the system is transformed back into the global coordinate system. The transformation of the incident direction, s', to the final direction, s, expressed in terms of Θ_s and Φ_s is given by:

$$\begin{pmatrix} s_x \\ s_y \\ s_z \end{pmatrix} = \begin{bmatrix} \frac{s'_x s'_z}{\sqrt{1-s'^2_z}} & \frac{s'_y}{\sqrt{1-s'^2_z}} & s'_x \\ \frac{s'_y s'_z}{\sqrt{1-s'^2_z}} & \frac{s'_x}{\sqrt{1-s'^2_z}} & s'_y \\ -\sqrt{1-s'^2_z} & 0 & s'_z \end{bmatrix} \begin{pmatrix} \sin\Theta_s \cos\Phi_s \\ \sin\Theta_s \sin\Phi_s \\ \cos\Phi_s \end{pmatrix} \tag{5.6}$$

Photon packets are launched from the input face of a cubic volume which represents the scattering medium and propagate through the system until they reach the volume boundary. At this point their properties are examined and those which meet the specified spatial and angular collection criteria are recorded. Detailed information for each photon packet can be tracked, including:

- position
- direction
- time-of-flight
- number of scattering events
- path length
- position of each interaction

5.2 Light propagation: Ray-tracing

The information tracked by the Monte Carlo code can lend insight into the aggregate effects of scattering from particles in turbid media. Applying this information to an imaging system, however, requires a detailed treatment of the optics which collect and filter the transmitted light and direct it to the detector.

To enable analysis of a complete system, a custom ray-tracing model was implemented which interfaces directly with the Monte Carlo results. This software was built using the Mathematica development environment and runs an adapted version of Rayica for geometric ray-tracing. This particular set of design tools was chosen to take advantage of an efficient commercial ray-tracing engine and existing component models, while maintaining full control over the design of non-standard optics, light sources, and the use of system resources. The ray-tracing model is contained in five main software components, which are written as Mathematica packages:

LundOptics This package defines 16 optical component models which can be used to represent the optical systems shown in Figs. 4.1, 4.7, 5.1, and 5.5.

LightFromFile This package interfaces with the Monte Carlo code and constructs light sources representing Monte Carlo data. The package defines 7 utility functions for loading, sorting, and saving Monte Carlo output and light source data. Optical components are defined in the Rayica formalism as a list of surfaces separated by material regions which are specified by a list of properties, including a detailed refractive index model.

StepTrace This package defines output display functions, and a wrapper class for the Rayica tracing engine, allowing large data files and to be processed incrementally. This is necessary due to memory constraints of the computer hardware used to execute the raytrace.

ResolutionTestChart This package defines 6 functions for generating light sources with specific spatial frequency characteristics for testing optical systems.

Contrast This package defines 5 functions for evaluating and viewing one-dimensional image contrast and discretizing raytracing intensity results.

The purpose of the raytracing code is to faithfully describe the collection optics of the BI optical system, allowing information from the Monte Carlo simulation to be filtered to reflect the spatial intensity incident on the detector in a physical BI system. Rays representing photon packets from the Monte Carlo calculations are generated and traced through the system optics to the output plane where they are integrated to form a spatial intensity profile. This geometric spatial intensity profile is then convolved with the a Gaussian kernel which models the diffraction limited spotsize [59] of the optical system. Time-gating effects are modeled by the light source which generates rays for the system, while the light collection restraints of the system geometry are enforced by the placement, clear aperture, and transmission characteristics of each component model.

Ray-tracing setup

The process to estimate the spatial intensity output from the Monte Carlo results follows the following procedure.

A component model is constructed for each optic in the BI system which specifies surface information, materials, and ray-tracing behavior. The component models are arranged in the system layout, and the system is aligned using rays from a Gaussian light source model.

The light source parameters for temporal filtering are chosen to model the action of time-gating in the system. Detection parameters are set for the dimensions of the detection plane in the coordinate system of the optics, and the discrete output array, which stores the integrated spatial intensity. The dimensions of the output array should be chosen based on the spatial resolution of the system and the spatial frequency content of the optical signal, respecting the Nyquist criteria[9], given by:

$$f_{\text{Nyquist}} = \frac{1}{2} \times \text{pixel spacing} \tag{5.7}$$

At this point the ray-tracing program defined by the StepTrace package is invoked, beginning an iterative procedure that loads and filters photon packet information from the Monte Carlo data and generates a set of rays which are traced through the system and summed to the output array. The summed result when all data have been processed is convolved with the diffraction-limited spotsize of the optics to yield the final image.

5.3 Image contrast enhancement

The system model output yields the spatial intensity imaged by the detector in a BI instrument. This result is useful for estimating the signal level produced by a given light collection arrangement, but further analysis is required to express the performance of the instrument as an imaging system.

The important aspect of an imaging system is it's ability to transmit spatial information. A useful parameter for evaluating performance in this respect is the visibility, or image contrast [19]. For a single spatial frequency, it is given by the ratio of the input modulation to the output modulation,

$$C = \frac{I_{\text{max}} - I_{\text{min}}}{I_{\text{min}} + I_{\text{max}}} \tag{5.8}$$

Where the contrast, C, is given by relating the minimum and maximum spatial intensities, I_{min} and I_{max}. Applying the contrast at all spatial frequencies yields the modulation transfer function which describes the optical response of the system.

By modulating the light source at different spatial frequencies and applying the system model to calculate the instrument response, a series of simulations can sample the contrast transfer function (CTF) of the modeled instrument, yielding a quantitative

metric for it's performance as an imaging system. In addition, the point-spread function, the irradiance produced by the instrument in response to a point source, can be calculated as the normalized modulus of the Fourier transform of the CTF.

5.4 Model validation

Previous work by Paciaroni [45] included spatial resolution measurements for a range of BI configurations, where the sytem contrast and point spread functions were measured over a range of extinction levels using suspensions of polystyrene microspheres in water. After these evaluations, Paciaroni and Linne settled on one of the tested designs, a variant of the time-gated instrument used by Alfano et al., as the most promising system for imaging in dense sprays. Paciaroni and Linne subsequently applied this system to image a turbulent water jet [46], a water jet in crossflow [36], and a transient diesel spray [37]. In 2006, this BI system was moved to Lund University and installed for the jet-in-crossflow measurements described in Sec. 4.1. The collection optics for this BI system are shown in Fig. 5.1.

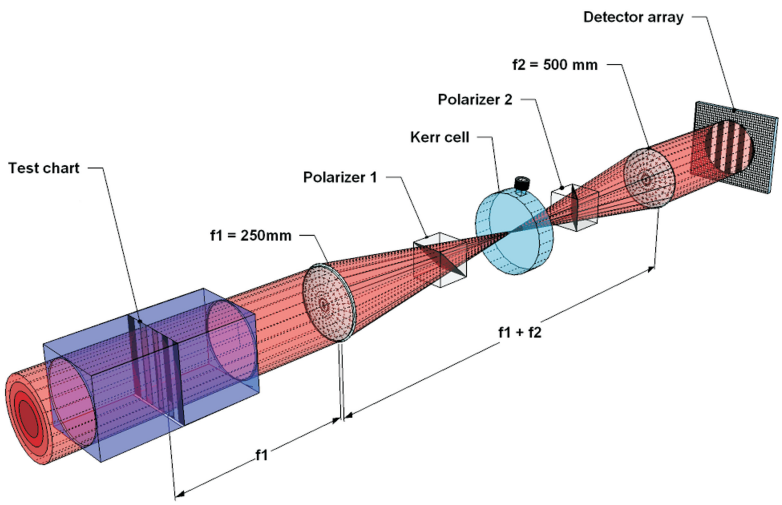

Figure 5.1: *Source projection light collection optics.*

Applying the system model to the optical arrangement and conditions used in Paciaroni's experimental characterization of the system provided a convenient test of the validity of the modeling results. In the simulation, the refractive indices of the distilled water and of the polystyrene spheres were set to 1.33 and 1.58 respectively. The scattering medium consisted of monodisperse microspheres with a diameter of 0.7 μm, and three different optical depths (OD = 5, 10, and 14) were investigated over spatial frequencies from 1 to 50 lp/mm. The scattering phase function representing this medium is shown in Fig. 5.7.

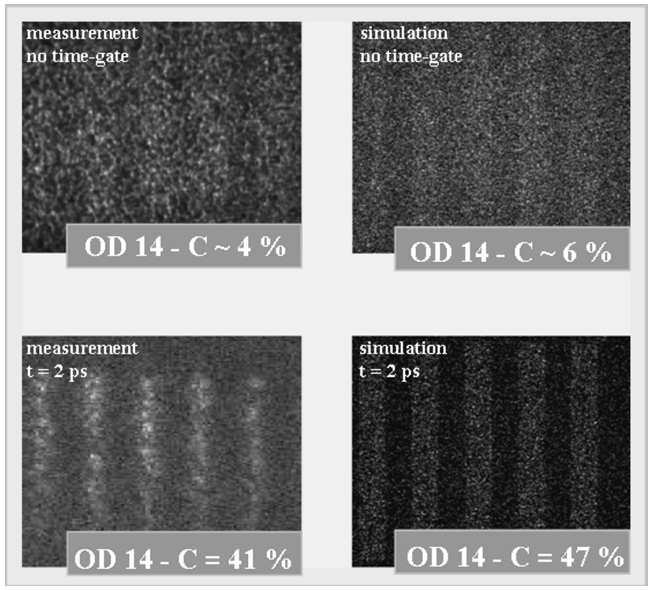

Figure 5.2: *Measurement/Simulation comparison: A resolution test chart bar pattern with a spatial frequency of 1 lp/mm is embedded in a scattering volume containing a solution of 0.7 μm spheres and imaged by the BI instrument. The measured images are shown on the left: no time-gating (top-left), ~2 ps time-gating (bottom-left). Simulation results for these experimental conditions are shown on the right: no time-gating (top-right), ~2 ps time-gating (bottom-right).*

Fig. 5.2 shows a side-by-side comparison of simulation results and ballistic imaging measurements of a resolution test chart embedded in the scattering volume, where OD = 14. Fig. 5.2(a) and 5.2(b) show results for the detected image when the Kerr-effect shutter is not present and the entire transmitted pulse is integrated by the detector.

In this case, the test pattern is barely discernible due to strong interference from diffusely scattered source light and the calculated contrast is on the order of 5%. The lower half of Fig. 5.2 shows measurement (left) and simulation (right) results obtained when the collected light is filtered by the action of the Kerr-effect shutter. Here the detected light is gated such that late-arriving (t > 2 ps) photons are excluded from the image, resulting in dramatically improved visibility of the test pattern, and a calculated contrast on the order of 55%.

Fig. 5.3 shows the contrast transfer functions of the BI sytem generated by the system model at each optical depth together with the measured transfer functions from Paciaroni and Fig. 5.4 shows the point spread functions derived from this CTF data. The simulated and measured values show good agreement and similar trends over the entire frequency range.

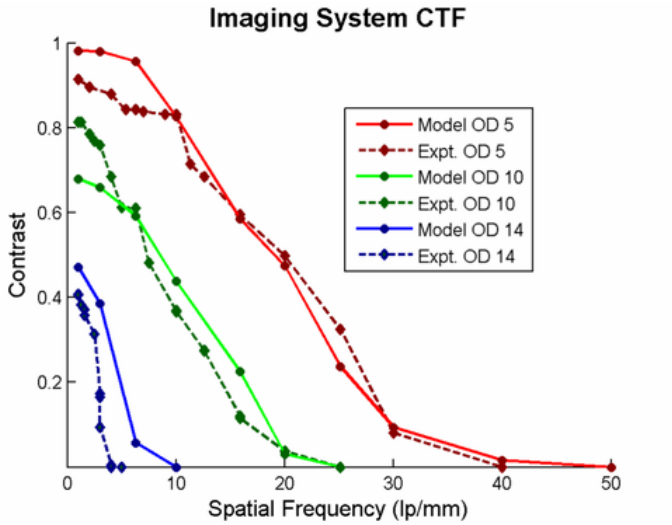

Figure 5.3: *Contrast transfer function for the source projection BI system and a scattering medium of 0.7 μm polystyrene spheres in water.*

The model can also be used to compare two imaging systems for a specific set of scattering conditions. Fig. 5.6 compares the action of time-gating on image contrast and intensity for the source projection system (red), shown in Fig. 5.1, and the source imaging system (blue), shown in Fig. 5.5. The scattering medium in both cases is represented by 0.7 μm polystyrene spheres in water, at OD = 14. Note that even for this high optical depth, the model shows the contrast tends to 100% when the width of the time-gate is reduced to very short times. However, this contrast improvement comes at the cost of a reduction in light intensity. For this particular set of conditions and spatial frequency (1 lp/mm) the source projection scheme (Fig. 5.1) outperforms the source imaging scheme (Fig. 5.5). This is consistent with discussion in Sec. 4.1 which predicted contrast improvement for the source projection scheme at low spatial frequencies.

The results shown here demonstrate that ballistic imaging has the potential, when properly applied, to significantly improve contrast in line-of-sight integrated images under optically dense conditions. The technique is effective in mitigating noise contributions, especially for large optical depths (OD = 10 and higher) where signals which are completely lost with no light discrimination may be recovered using appropriate spatial and temporal filtering. Since the light scattering properties of the measurement volume and the light selection capacity of the BI system are interdependent, the system model introduced in this chapter represents an essential tool for optimizing the BI instrument to yield the best results for the specific scattering environment under investigation.

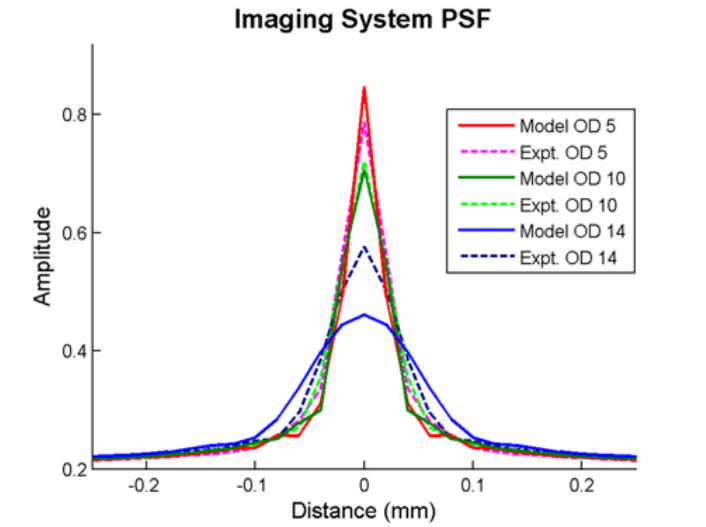

Figure 5.4: *Point spread function for the source projection BI system and a scattering medium of 0.7 μm polystyrene spheres in water.*

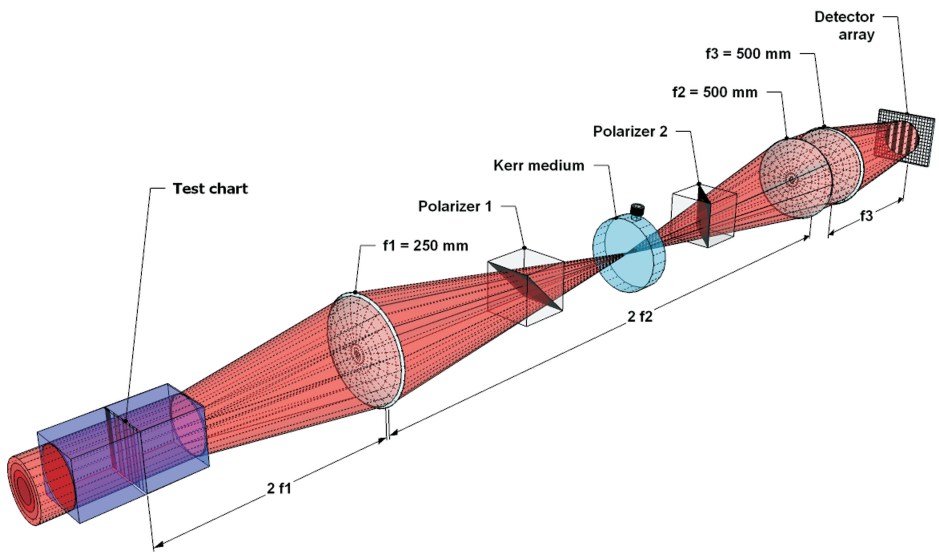

Figure 5.5: *Source imaging light collection optics.*

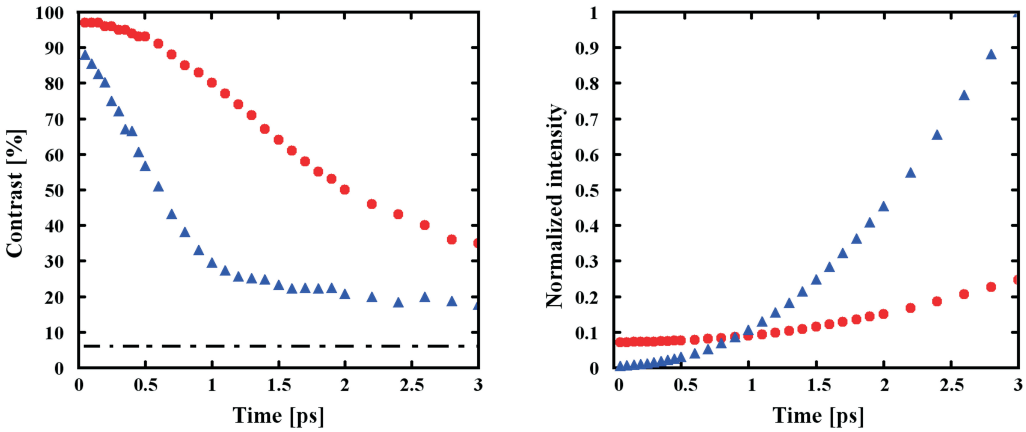

Figure 5.6: *Comparison of source projection (red) and source imaging (blue) BI instruments. Scattering conditions: OD = 14, 0.7 μm scatterers, spatial frequency = 1 lp/mm.*

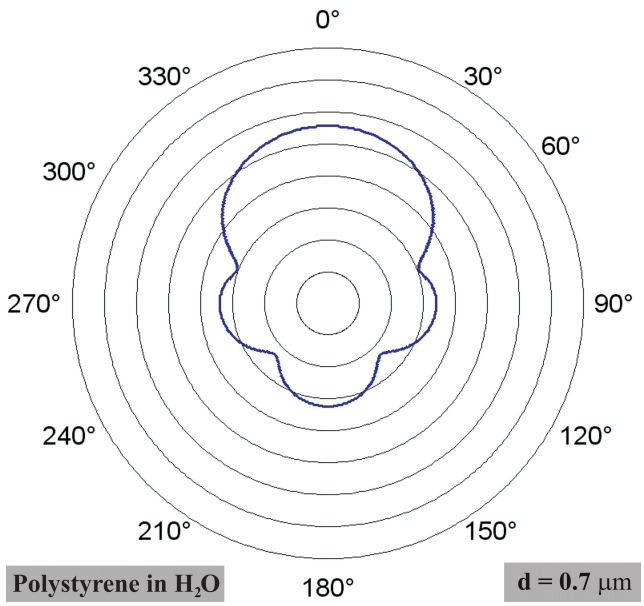

Figure 5.7: *Scattering phase function for polystyrene spheres in water, d = 0.7 μm.*

Chapter 6

Conclusions

This thesis presents ballistic imaging measurements, analysis of experimental results, and modeling work focused on understanding the scattering and light collection related to BI measurements.

The first set of experiments applied BI to a jet-in-crossflow relevant to gas turbine fuel injection. Images of this spray were acquired with well-qualified boundary conditions resulting in a data set suitable for spray model validation. Results of this study reveal bifurcation occurring in the two-phase spray caused by interactions between the liquid jet and the gaseous crossflow. This represents the first observation of bifurcation in a two-phase system, and has implications for improving fuel injection by accelerating spray breakup and mixing.

The second set of experiments applied a modified BI system to an aerated spray, where breakup was enhanced by the addition of small quantities of gas upstream of the nozzle orifice. This spray was studied over a wide range of flowrates and gas-to-liquid ratios. The results of this study reveal a dependence on the overall flowrate for achieving the breakup modes normally associated with aerated sprays; a result which has not previously been reported in the effervescent spray literature.

Measuring velocity in a dense spray is a significant challenge due to the high variability of the flow structure and the distortion and attenuation of optical signals by scattering. Time-gated ballistic images from both sets of spray measurements were examined using correlation methods; first applied to a single falling drop, and later applied to track velocities in a full spray. This work showed that BI diagnostics can offer image contrast improvements sufficient to enable correlation analysis in dense sprays. By implementing this analysis, together with targeting methods based on image structure, this work demonstrated the first application of BI as a velocity measurement applicable to dense sprays.

Further development of BI, where the instrument is adapted and optimized to different kinds of imaging conditions requires a detailed understanding of light scattering and the collection optics of the system. The modeling effort in this work was undertaken to facilitate this understanding and provide a tool for directly comparing and optimiz-

ing BI instruments. A flexible BI system model was implemented and validated against previous experimental work, showing excellent agreement with BI measurements.

A significant advantage of the system model is the ability to easily test parameters which are sensitive or otherwise difficult to vary in an experimental context. For example, Paper VII examines spatial and temporal profiles of distinct scattering orders, where photon information is sorted based on the number of interactions encountered by each photon packet as it transits the medium. Precise filtering of light in this manner is simply not feasible in a physical measurement. In this case, investigation of light collected in each scattering order reveals an unusual property unique to forward scattering: that the temporal and spatial profiles of individual scattering orders is independent of the number density of scatterers. This means that even though the magnitude of each order will vary, the information transmitted by each scattering order is independent of optical depth for any set geometry.

Future work should explore this capacity, applying the model to well-characterized turbid media and analyzing the results for broader trends that extend beyond a narrow range of scattering conditions. In particular, the system model offers the opportunity to completely analyze light scattering in a quasi-deterministic fashion by tracking every photon packet. For a very simple test image, this could enable classification of photons strictly based on the value of their contributon to an image, in effect sorting transmitted light in absolute terms. These absolute classes could then be compared directly with experimentally viable sorting techniques such as time-gating or spatial filtering, to determine the real accuracy of these filtering mechanisms, possibly leading to a functional theoretical basis for the aggregate effects of light scattering in this context.

Ballistic imaging is a promising diagnostic for measurements highly turbid media. Coupled with the understanding of the aggregate effects of light scattering provided by the system model, BI can now be optimized for specific scattering situations, and has the potential to directly address important questions in combustion, fuel injection, and other applications that require high-resolution imaging in optically dense environments.

Greek alphabet

A	α	alpha
B	β	beta
Γ	γ	alpha
Δ	δ	delta
E	ϵ	epsilon
Z	ζ	zeta
H	η	eta
I	ι	iota
K	κ	kappa
Λ	μ	lambda
M	μ	mu
N	ν	nu
Ξ	ξ	xi
O	o	omicron
Π	π	pi
P	ρ	rho
Σ	σ	sigma
T	τ	tau
Υ	υ	upsilon
Φ	ϕ	phi
X	χ	chi
Ψ	ψ	psi
Ω	ω	omega

Acknowledgements

This thesis was mainly carried out at Lund University in the Division of Combustion Physics. I was also fortunate enough to have the opportunity to pursue projects at the Technical University of Darmstadt in Germany, Cranfield University in the U.K., and Wright-Patterson AFB in the U.S. Each of these projects were beneficial in my thesis work, but even more valuable were the experiences I had and the people I worked with in each of these research groups. Over the course of this thesis I have had rewarding contacts with many people and to each of them I am sincerely grateful. I would like to express particular appreciation to a few of the people that have helped me in the completion of this thesis.

I would like to thank my thesis advisor Professor *Mark Linne* whom I've had the pleasure of knowing since the beginning of my undergraduate career. His understanding of physics, teaching philosophy, and enthusiastic approach to research have been an inspiration and an invaluable resource. Without his encouragement and assistance this thesis would not have been possible.

I would also like to express my appreciation to Professor *Marcus Aldén*, Head of the Division of Combustion Physics. My experience in Lund has been fantastic from the very beginning, thanks in large part to his hard work and deep commitment to making the Division an open and exciting place to work.

I am grateful to *Megan Paciaroni*, for many hours of help and technical assistance in the lab, and even more for her wit, unique perspectives, and fueling my appreciation for classical music. I would like to thank *Edouard Berrocal* for many interesting and fruitful discussions and collaborations, both in Lund and at Cranfield. The success of the model presented in this work is due in no small measure to his enthusiasm and help in implementing the Monte Carlo code.

I would like to thank Professor *Per-Erik Bengstsson*, especially for his helpful advice and guidance with the CARS technique early in my thesis work. I am grateful to *Frederik Ossler* for his advice on X-ray and neutron scattering, and for generously sharing music that is perfect for late nights in the lab.

I would like to thank Professor *Andreas Dreizler* for hosting me at his lab in Darmstadt, and for many fruitful discussions.

I am very grateful *James Gord* and *Campbell Carter* for support and advice during several measurement campaigns at the Air Force research lab in Dayton, Ohio. I would also like to thank *Sukesh Roy* for his help and interesting discussions during my time at

Wright-Patterson AFB.

I would like to thank *Igor Meglinski* for supporting my short stay in Cranfield and for insightful discussions on light scattering.

I am sincerely grateful to *Mikhael Afzelius*, *Thomas Metz*, and *Joakim Walewski* for their help getting started on my work at the Division, and getting settled into life in Lund.

I would like to thank *Per Petersson* for his advice and collaboration on PIV and LDV measurements, and for the good times we shared during coursework in Gothenburg and Stockholm, and as officemates for the past four years. I thank *Erich Wachter* for his help in understanding LES and for a lot of good times in Germany and Denmark.

I would like to thank *Christian Brackmann* for his help analyzing CARS data, and *Fredrik Vestin* and *Robert Collin* for their collaboration on CARS in the high-pressure burner. I would like to thank *Johan Zetterberg* for introducing me to filtered Rayleigh measurements and for many interesting discussions having little to do with physics. I would like to thank *Joakim Bood* and *Zhongshan Li* for discussions on spectroscopy and general physics that were always full of creative ideas for improving diagnostics.

I am thoroughly indebted to the Division staff who have helped me constantly, it seems, with problems great and small throughout my time here. In particular I want to thank technicians *Rutger Lorensson* and *Thomas Wendel* for their excellent advice and craftsmanship, and administrators, *Eva Persson*, *Marie Persson*, *Elna Brodin*, *Nina Mårtensson* and *Sara Holmgren*.

I would like to particularly thank *Anneli Nilsson* and *Cecilia Bille* for their tremendous help in keeping me on track and financed, and for making the Division such an efficient and fun place to work.

I would like to thank my colleagues in the physics department that I haven't been able to work with directly, but nonetheless have enriched my experience at the Division through their own excellent work and pleasant company. In particular I would like to mention *Hans Seyfried, Andreas Ehn, Jimmy Olofsson, Alaa Omrane, Gustaf Särner, Martin Linvin, Andreas Lantz, Jonathan Johnsson Elias Kristensson, Billy Kalvdee, Johan Sjöholm, Olof Johansson, Andreas Arvidsson, and Johannes Lindén.* To the rest of you whose presence has been important, both within and outside the Division, whom I have not mentioned by name, I also express my sincere appreciation.

In closing, I would like to thank my family for their continual support and understanding which has always been a source of strength and comfort.

References

[1] Nils H. Abramson and Kenneth G. Spears. 1989. Single pulse light-in-flight recording by holography. *Applied Optics*, 28(10):1834–1841.

[2] R. R. Alfano, S. G. Demos, and S. K. Gayen. 1997. Advances in optical imaging of biomedical media. *Annals of the New York Academy of Sciences*, 820:248–271.

[3] M. Bashkansky, C. L. Adler, and J. Reintjes. 1994. Coherently amplified raman polarization gate for imaging through scattering media. *Optics Letters.*, 19(5): 350–2.

[4] Edouard Berrocal. 2006. *Multiple scattering of light in optical diagnostics of dense sprays and other complex turbid media*. PhD thesis, Cranfield University, Cranfield, UK.

[5] Craig F. Bohren and Donald R. Huffman. 1983. *Absorption and scattering of light by small particles*. Wiley. ISBN 047105772X.

[6] Max Born and Emil Wolf. 1970. *Principles of optics*, 4 edition. Pergamon Press. ISBN 0080139876.

[7] Robert W. Boyd. 2008. *Nonlinear optics*, 3 edition. Academic Press. ISBN 9780123694706.

[8] H. P. Chiang, W. S. Chang, and J. Wang. 1993. Imaging through random scattering media by using cw broadband interferometry. *Optics Letters*, 18(7):546–8.

[9] Robert L. Cook. 1986. Stochastic sampling in computer graphics. *ACM Transactions on Graphics*, 5(1):51–72. ISSN 0730-0301.

[10] S. G. Demos and R. R. Alfano. 1996. Temporal gating in highly scattering media by the degree of optical polarization. *Optics Letters.*, 21(2):161–163.

[11] M. A. Duguay and J. W. Hansen. 1969. An ultrafast light gate. *Applied Physics Letters*, 15(6):192–194.

[12] M. A. Duguay and A. T. Mattick. 1971. Ultrahigh speed photography of picosecond light pulses and echoes. *Applied Optics*, 10(9):2162–2170.

[13] M. D. Duncan, R. Mahon, L. L. Tankersley, and J. Reintjes. 1991. Time-gated imaging through scattering media using stimulated raman amplification. *Optics Letters.*, 16(23):1868–70.

[14] C. Dunsby and P. M. W. French. 2003. Techniques for depth-resolved imaging through turbid media including coherence-gated imaging. *Journal of Physics D: Applied Physics*, 36(14):R207–27.

[15] Olivier Emile, Fabien Bretenaker, and Albert Le Floch. 1996. Rotating polarization imaging in turbid media. *Optics Letters*, 21(20):1706–1708.

[16] P. A. Galland, X. Liang, and L. Wang. 1995. Time-resolved optical imaging of jet sprays and droplets in highly scattering medium. In *Proceedings of the American Society of Mechanical Engineers*, volume HTD-321, pages 585–8.

[17] Venkatesh Gopal, Sushil Mujumdar, Hema Ramachandran, and A. K. Sood. 1999. Imaging in turbid media using quasi-ballistic photons. *Optics Communications*, 170(4-6):331 – 345. ISSN 0030-4018.

[18] C. G. Gray and B. G. Nickel. 1978. Debye potential representation of vector fields. *American Journal of Physics*, 46(7):735–736.

[19] Eugene Hecht. 1998. *Optics*, 3 edition. Addison-Wesley Publishing Company, Reading, Massachusetts. ISBN 0201838877.

[20] P. P. Ho and R. R. Alfano. 1979. The optical kerr effect in liquids. *Phys. Rev. A*, 20(5):2170–87.

[21] Hiromichi Horinaka, Koji Hashimoto, Kenji Wada, Yoshio Cho, and Masahiko Osawa. 1995. Extraction of quasi-straightforward-propagating photons from diffused light transmitting through a scattering medium by polarization modulation. *Optics Letters*, 20(13):1501–3.

[22] B. K. P. Horn and B. G. Shunck. 1981. Determing optical flow. *Artificial Intelligence*, 17:185–203.

[23] S. C. W. Hyde, N. P. Barry, R. Jones, and P. M. W. French. 1996. High resolution depth resolved imaging through scattering media using time resolved holography. *Optics Communications*, 122(4):111–6.

[24] Saïd Idlahcen, Loïc Méès, Claude Rozé, Thierry Girasole, and Jean-Bernard Blaisot. 2009. Time gate, optical layout, and wavelength effects on ballistic imaging. *J. Opt. Soc. Am. A*, 26(9):1995–2004.

[25] A. Ishimaru. 1978. *Wave propagation and scattering in random media*. Academic Press. ISBN 0123747015.

[26] John David Jackson. 1962. *Classical Electrodynamics*. Wiley.

[27] L. L. Kalpaxis, L. M. Wang, P. A. Galland, and R. R. Alfano. 1993. Three-dimensional temporal image reconstruction of an object hidden in highly scattering media by time-gated optical tomography. *Optics Letters*, 18(20):1691–3.

[28] D. H. Kelly. 1965. Spatial frequency, bandwidth, and resolution. *Applied Optics*, 4(4):435–435.

[29] S. Kielich. 1972. Nonlinear optical and electro-optical properties of dielectrics and ferroelectrics. *Ferroelectrics*, 4:257–282.

[30] A. H. Lefebvre. 1989. *Atomization and Sprays*. Taylor and Francis, New York, NY. ISBN 0891166033.

[31] Emmett N. Leith, C. Chen, and H. Chen. 1992. Imaging through scattering media with holography. *Journal of the Optical Society of America A*, 9(7):1148–53.

[32] Emmett N. Leith, C. Chen, H. Chen, Y. Chen, J. Lopez, P. C. Sun, and D. Dilworth. 1991. Imaging through scattering media using spatial incoherence techniques. *Optics Letters*, 16(23):1820–1822.

[33] Emmett N. Leith and Juris Upatnieks. 1962. Reconstructed wavefronts and communication theory. *Journal of the Optical Society of America*, 52(10):1123–1128.

[34] X. Liang, L. Wang, P. P. Ho, and R. R. Alfano. 1995. Two-dimensional kerr—fourier imaging of translucent phantoms in thick turbid media. *Applied Optics*, 34(18):3463–3467.

[35] X. Liang, L. Wang, P. P. Ho, and R. R. Alfano. 1997. Time-resolved polarization shadowgrams in turbid media. *Applied Optics*, 36(13):2984–2989.

[36] Mark A. Linne, Megan E. Paciaroni, James R. Gord, and Terrence R. Meyer. 2005. Ballistic imaging of the liquid core for a steady jet in crossflow. *Applied Optics*, 44: 6627–34.

[37] Mark A. Linne, Megan E. Paciaroni, T. Hall, and T. Parker. 2006. Ballistic imaging of the near field in a diesel spray. *Experiments in Fluids*, 40(6):836–46.

[38] J. G. Liu and H. Yan. 2008. Phase correlation pixel-to-pixel image co-registration based on optical flow and median shift propagation. *International Journal of Remote Sensing*, 29(20):5943–5956.

[39] R. Mahon, M. D. Duncan, L. L. Tankersley, and J. Reintjes. 1993. Time-gated imaging through dense scatterers with a raman amplifier. *Applied Optics*, 32(36): 7425–33.

[40] Jerry B. Marion and Stephen T. Thornton. 1995. *Classical dynamics of particles and systems*, 4 edition. Saunders College Publishing. ISBN 0030973023.

[41] J. Martin, Y. Lecarpentier, A. Antonetti, and G. Grillon. 1980. Picosecond laser stereometry light scattering measurements on biological material. *Medical and Biological Engineering and Computing*, 18(2):250–2.

[42] Marvin Minsky. 1955. Confocal scanning microscope. Rapport technique. Patent 3,013,467.

[43] Ivan Moreno. 2004. Jones matrix for image-rotation prisms. *Applied Optics*, 43 (17):3373–3381.

[44] N. Otsu. 1979. A threshold selection method from gray-level histograms. *IEEE Transactions on Systems, Man, and Cybernetics*, 9(1):62–66.

[45] Megan E. Paciaroni. 2004. *Time-gated ballistic imaging through scattering media with applications to liquid spray combustion*. PhD thesis, Division of Engineering, Colorado School of Mines, Golden, CO.

[46] Megan E. Paciaroni, T. Hall, J. P. Delplanque, T. Parker, and Mark A. Linne. 2006. Single-shot two-dimensional ballistic imaging of the liquid core in an atomizing spray. *Atomization Sprays*, 16:51–70.

[47] Megan E. Paciaroni and Mark A. Linne. 2004. Single-shot two-dimensional ballistic imaging through scattering media. *Applied Optics*, 43:5100–9.

[48] J. D. Posner, D. Dunn-Rankin, M. S. Brown, N. Brock, and P. A. DeBarber. 2004. Resonant holographic interferometry for species concentration measurements with saturated anomalous dispersion. *Applied Physics B: Lasers and Optics*, 78(6):661–672.

[49] J. Reintjes, M. Bashkansky, and M. D. Duncan. 1993. Time-gated imaging with nonlinear optical raman interactions. *Optics and Photonics News*, 4(10):28–32.

[50] Christian Ronse. 1998. Set-theoretical algebraic approaches to connectivity in continuous or digital spaces. *Journal of Mathematical Imaging and Vision*, 8(1): 41–58.

[51] K. Sala and M. C. Richardson. 1975. Optical kerr effect induced by ultrashort laser pulses. *Phys. Rev. A*, 12(3):1036–47.

[52] Vanitha Sankaran, Klaus Schönenberger, Jr. Joseph T. Walsh, and Duncan J. Maitland. 1999. Polarization discrimination of coherently propagating light in turbid media. *Applied Optics*, 38(19):4252–4261.

[53] P. J. Santangelo and P. E. Sojka. 1994. Focused-image holography as a dense-spray diagnostic. *Applied Optics*, 33(19):4132–4136.

[54] A. Sappey. 1994. Optical imaging through turbid media with a degenerate four wave mixing correlation time gate. *Applied Optics*, 33(36):8346–54.

[55] S. D. Sovani, J. D. Crofts, P. E. Sojka, J. P. Gore, and W. A. Eckerle. 2005. Structure and steady-state spray performance of an effervescent diesel injector. *Fuel*, 84 (12-13):1503–1514.

[56] Karl A. Stetson. 1967. Holographic fog penetration. *Journal of the Optical Society of America*, 57(8):1060–1061.

[57] P. T. Tokumaru and P. E. Dimotakis. 1995. Image correlation velocimetry. *Experiments in Fluids*, 19:1–15.

[58] J. Scott Tyo. 2000. Enhancement of the point-spread function for imaging in scattering media by use of polarization-difference imaging. *Journal of the Optical Society of America A*, 17(1):1–10.

[59] Hakan Urey. 2004. Spot size, depth-of-focus, and diffraction ring intensity formulas for truncated gaussian beams. *Applied Optics*, 43(3):620–625.

[60] H. C. van de Hulst. 1981. *Light scattering by small particles*, 2 edition. Dover, N.Y. ISBN 0486642283.

[61] L. Wang, P. P. Ho, and R. R. Alfano. 1993. Double-stage picosecond kerr gate for ballistic time-gated optical imaging in turbid media. *Applied Optics*, 32(4): 535–40.

[62] L. Wang, P. P. Ho, X. Liang, and R. R. Alfano. 1993. Kerr-fourier imaging of hidden objects in thick turbid media. *Optics Letters*, 18(3):241–3.

[63] Q. Z. Wang, X. Liang, L. Wang, and R. R. Alfano. 1995. Fourier spatial filter acts as a temporal gate for light propagating through a turbid medium. *Optics Letters*, 20(13):1498–1500.

[64] J. Watson, P. Georges, T. Lepine, and A. Brun. 1995. Imaging in diffuse media with ultrafast degenerate optical parametric amplification. *Optics Letters*, 20(3): 231–3.

[65] K. M. Yoo, Qirong Xing, and R. R. Alfano. 1991. Imaging objects hidden in highly scattering media using femtosecond second-harmonic-generation cross-correlation time gating. *Optics Letters*, 16(13):1019–1021.

Summary of Papers

I. This paper reviews the development of Ballistic Imaging applications for sprays and transient phenomena relevant to combustion. Ballistic imaging is introduced and specific applications for diagnostics of primary breakup processes are discussed, including: a LOX injector, a turbulent water jet, a water jet in cross-flow, a transient diesel fuel spray, a rocket fuel injector, and an aerated spray. The paper further describes detailed studies of photon transmission through dense media and discusses incorporation of those results into a model for a ballistic imaging instrument to evaluate and optimize the diagnostic.

Mark Linne planned the paper and compiled the manuscript from contributions from Megan Paciaroni, Edouard Berrocal and myself. Megan Paciaroni, Joseph Zelina, and I made the jet-in-crossflow measurements and I developed the software used to analyze these spray images for breakup and drop size statistics. I planned and conducted the aerated spray measurements and developed the software used to analyze these spray images and extract velocity information. Edouard Berrocal and I planned and implemented the numerical model for the ballistic imaging instrument.

II. This paper presents results from ballistic imaging, as well as particle imaging velocimetry and high speed shadowgraphy, applied to a liquid jet in a crossflow of air under a variety of conditions. The experimental system was designed to provide well controlled conditions with minimal amounts of turbulence in the liquid jet and the gaseous crossflow. A variety of Weber numbers and the momentum flux rations were studied in order to provide a sizeable data set for the validation of computational models. The paper briefly describes each imaging technique, outlines the results obtained, and tabulates image statistics for each of 10 spray conditions at varying distances from the spray nozzle orifice.

Mark Linne, Megan Paciaroni, Joseph Zelina, and I planned the experiments. Megan Paciaroni designed and built the spray and the crossflow channel. Megan Paciaroni, Joseph Zelina and I conducted the experimental work, excepting the PIV measurements, which were carried out by Per Petersson. I designed the analysis software used to compile the image statistics. Mark Linne, Megan Paciaroni, and I developed the manuscript.

III. In this paper ballistic imaging is applied to the near nozzle region of a high pressure effervescent atomizer to investigate the mechanisms which dominate liquid breakup. This technique has revealed various breakup regimes which exhibit dependence on the total flow rate and the gas-to-liquid ratio (GLR). At low total speeds, the jet does not develop the wide spread angle and rapid breakup for which effervescent sprays are known, even at high GLR. Above a distinct threshold for total flow rate, the jet passes through several distinctive flow regimes which vary with GLR and the spray does achieve the expected wide spread angle and rapid breakup. Intermediate GLR's produce interesting flow patterns, apparently generated by surging at the nozzle exit. This surging is attributed to the flow pattern of the liquid just as it exits the nozzle. Specific interior flows seem to generate the most rapid breakup and warrant further investigation.

I planned the experiments and carried out the measurements based on advice by Mark Linne, James Gord, Terry Meyer, and Campbell Carter. The effervescent spray equipment was designed and built by Campbel Carter's research group at the Air Force Research Laboratory. Mark Linne developed the text and I prepared the spray images for the manuscript.

IV. This paper presents analysis of a pair of ballistic images which capture the dynamics of a compound water droplet as it falls a short distance over a 1 ms time-frame. Edge detection, image segmentation, and correlation analysis algorithms are employed to extract velocity information from the images. The method is shown to be effective for tracking liquid phase droplet features within the resolution limit of the imaging system. In light of these results, an extension of the technique to a three-image implementation is discussed, which would allow the determination of acceleration, and facilitate quantitative estimation of the forces active in liquid breakup.

Mark Linne planned the experiment. Megan Paciaroni, Terry Meyer, and Mark Linne conducted the measurements. I designed the image processing software, conducted the velocity analysis, and prepared the manuscript.

V. This paper details the implementation of a targeted correlation method for determining the velocity of liquid structures within a turbulent spray. Ballistic imaging was applied to an aerated water spray, and pairs of ballistic images with a time separation of 10 μs were recorded. The paper presents the first ballistic images of a novel liquid-fuel injector for scramjet combustion, and the first velocity information from ballistic images relevant to breakup in the near-field of a spray.

Mark Linne, James Gord, Terry Meyer, and I planned the experiments. Terry Meyer and I conducted the measurements. The spray equipment was provided by Campbel Carter's research group. I developed the targeted correlation method, designed the image analysis software, carried out the velocity analysis, and prepared the manuscript.

VI. This paper investigates the scattering of an ultrashort laser pulse through homogeneous solutions of monodisperse polystyrene spheres. The two-dimensional distribution of light intensity was measured experimentally, and calculated via Monte Carlo simulation for both forward and side scattering. Contributions from each scattering order to the total detected light intensity were quantified for a range of different scattering phase functions, optical depths, and detection acceptance angles. Results demonstrate good agreement between the experimental and simulated results. Additionally, an extrapolation of the Beer-Lambert law to multiple scattering is proposed based on the Monte Carlo calculation of the ballistic photon contribution to the total detected light intensity.

Mark Linne, Edouard Berrocal, Megan Paciaroni and I planned the work. Edouard Berrocal, Megan Paciaroni, and I made the measurements. Edouard Berrocal implemented the code for the simulations and analyzed the data. Edouard Berrocal and I prepared the manuscript.

VII. This paper builds on the work presented in a previous paper where agreement between experimental measurements and results from Monte Carlo simulations were demonstrated for the spatial intensity distribution of a laser beam propagating within a turbid environment. In this installment, the validated Monte Carlo model is used to investigate spatial and temporal effects from distinct scattering orders on image formation. The contribution of ballistic photons and the first twelve scattering orders are analyzed individually by filtering the appropriate data from simulation results in both side-scattering and forward-scattering detection geometries. Results show the distribution of positions for final scattering events is independent of particle concentration when considering any individual scattering order in the forward detection. From this observation, it follows that the normalized intensity distribution of each order, in both space and time, is independent of the number density of particles. As a result, the amount of transmitted information is constant for a given scattering order and is directly related to the phase function in association with the detection acceptance angle.

Edouard Berrocal and I planned the simulations, interpreted the results, and prepared the manuscript. Edouard Berrocal implemented the code for the simulations and prepared the data and figures for the paper.

VIII. This paper demonstrates the ability of a BI system to mitigate image noise from multiply-scattered light, resulting in an imaging system with improved contrast which can resolve internal fluid structures in sprays where a dense fog of droplets significantly distorts the optical signal. The BI system is analyzed using a numerical model in which light propagation in the spray is treated by a Monte Carlo solution to photon transport and coupled to a raytracing model which treats the full system optics. Model results are validated against earlier experimental work using polystyrene spheres in water at an optical depth of 14, and show good agreement with the measured results. The model is then applied to a polydisperse distribution of fuel droplets with a representative Sauter mean diameter, $d_{32} = 23\mu$m,

demonstrating how the quantitative predictions of the model allow the effectiveness of both the spatial and temporal filtering of the BI instrument to be estimated. Applying the model to the spray reveals that the spatial filtering and time gating effects of the BI system improve image contrast, revealing information that is not available with conventional imaging techniques.

Edouard Berrocal, Mark Linne, and I planned the simulations. Edouard Berrocal and I implemented the code for the simulations, interpreted the results, and prepared the manuscript.